Determination of Longwave Heat Flux at the Air–Sea Interface Using Measurements from Buoy Platforms*

T. D. DICKEY AND D. V. MANOV

University of Southern California, Los Angeles, Los Angeles, California

R. A. WELLER

Woods Hole Oceanographic Institution, Woods Hole, Massachusetts

D. A. SIEGEL

University of California at Santa Barbara, Santa Barbara, California

(Manuscript received 22 February 1993, in final form 22 November 1993)

ABSTRACT

A theory for pyrgeometer operation is utilized for determining downwelling longwave radiation. Errors in downwelling longwave radiation measurements are due to differences in pyrgeometer body and dome temperatures compared to that of the atmosphere. Additionally, incident shortwave radiation fluxes may be important. Using the present theory along with laboratory and field observations, it appears that downwelling longwave heat fluxes can be measured with errors less than 6 W m^{-2}. Longwave heat flux observations from surface buoys deployed in four different oceanic regions suggest that 1) incoming longwave measurements from buoys are repeatable, 2) uncertainties in radiometer calibration are significant and systematic, and 3) pyrgeometers are affected by direct and indirect solar heating. A hybrid measurement method for the determination of net longwave heat flux at the air–sea interface is described. The authors recommend improvement in calibration procedures as well as development of a radiometer to be used as a transfer standard to compare with in situ measurements. Uncertainties in sea surface skin temperature and emissivity are contributors to the error in the net longwave heat flux. However, a targeted error limit goal of ±10 W m^{-2} for the monthly mean net longwave heat flux appears to be achievable.

1. Introduction

The fundamental and compelling needs for accurate air–sea flux estimates have been discussed by various authors including Weller and Hosom (1989), Donelan (1990), and Weller et al. (1991a,b). One of the important goals of the World Ocean Circulation Experiment (WOCE) is to utilize determinations of air–sea heat and momentum fluxes for driving ocean general circulation models. In addition, the heat flux determinations are important for addressing climate issues.

The heat flux budget at the sea surface may be expressed as

$$Q = \mathrm{SW}\Updownarrow + \mathrm{LW}\Updownarrow + Q_S + Q_L, \qquad (1)$$

where Q is the net surface heat flux across the air–sea interface, SW⇅ is the net shortwave heat flux, LW⇅ is the net longwave heat flux, Q_S is the sensible heat flux, and Q_L is the latent heat flux. The net longwave heat flux LW⇅ is the primary focus of this work. Climatological heat flux budget studies have shown that LW⇅ is generally the third largest term in the mean heat flux budget at midlatitudes (e.g., Dorman et al. 1974; Bunker 1976; Fung et al. 1984; Smith and Dobson 1984). However, its magnitude may at times be larger than the latent heat flux. It should be noted that the relative importance of the net longwave component varies with geographic location and time, particularly seasonally and diurnally.

To achieve the goals of global ocean circulation and climate experiments such as WOCE and the Tropical Ocean Global Atmosphere (TOGA) experiment, the targeted accuracy for each of the air–sea heat flux components is ±10 W m^{-2} for the monthly mean and longer timescales (Weller and Hosom 1989; WOCE 1985, 1989). The accuracy goal for the net air–sea heat flux Q is ±30 W m^{-2} for these same timescales. These demanding limits require that the accuracies of all of the components of the net surface heat flux budget be improved. Among the poorest accuracies are those of

* WHOI Contribution No. 8273.

Corresponding author address: Dr. T. D. Dickey, Ocean Physics Group, Department of Geological Sciences, University of Southern California, Los Angeles, CA 90089-0740.

the net longwave heat flux (LW$\Uparrow\Downarrow$). For example, monthly mean deviations among estimates based upon several different parameterization formulations and radiative transfer calculations are as great as ± 35 W m^{-2} (Chou 1985). Some observations indicate deviations between direct observations of LW$\Uparrow\Downarrow$ and bulk formula determinations of ± 20–25 W m^{-2} on shorter timescales (Siegel and Dickey 1986).

The net shortwave heat flux SW$\Uparrow\Downarrow$ is commonly defined to be the net solar radiation flux for wavelengths between 0.3 and 3 μm, while wavelengths between 3 and 50 μm comprise LW$\Uparrow\Downarrow$. The net all-wave heat flux is defined as SW$\Uparrow\Downarrow$ + LW$\Uparrow\Downarrow$. The net shortwave radiation SW$\Uparrow\Downarrow$ is the difference between the downwelling radiation from the sun as modified by the gases and clouds of the atmosphere and the radiation returned from the sea surface, which is either reflected by the surface or backscattered from within the water column. The net longwave heat flux LW$\Uparrow\Downarrow$ is the net flux of the greybody emissions from the sea surface, cloud layers, and the gases of the atmosphere. Since the sea surface is generally warmer than the atmosphere above it, LW$\Uparrow\Downarrow$ is usually negative, that is, emitted from the sea surface to the atmosphere.

The present work focuses on the determination of the net longwave heat flux component of the sea surface heat flux budget using buoy (and in principle shipboard) mounted sensors. Few direct measurements such as these have been made. The difficulties associated with the determination of this component are described in several relevant references (e.g., Katsaros 1980, 1990; Breon et al. 1991).

There are four primary methods that have been used to estimate LW$\Uparrow\Downarrow$ from surface-based measurements. These include direct measurements using a radiometer designed to measure the net longwave heat flux (e.g., Paltridge 1969, 1970; Simpson and Paulson 1979; Siegel and Dickey 1986; Halldin and Lindroth 1992), indirect determination using differences between the net all-wave and net shortwave heat fluxes (e.g., Reed and Halpern 1975; Reed 1976; Simpson and Paulson 1979), and parameterization of LW$\Uparrow\Downarrow$ using observed meteorological parameters (e.g., bulk parameterization method: Bunker 1976; Reed 1976; Simpson and Paulson 1979; Fung et al. 1984; Siegel and Dickey 1986). Finally, hybrid techniques have been developed. For example, the downwelling longwave flux may be measured directly and the upwelling flux may be parameterized (Lind et al. 1984; Lind and Katsaros 1986a,b).

The present study was part of the Improved Meteorological Measurements from Buoys and Ships (IMET) program. The overall objective of the IMET program was to develop meteorological instrumentation systems for obtaining accurate, reliable, and readily available determinations of heat and momentum fluxes across the air–sea interface (Weller and Hosom 1989; Prada et al. 1989, 1990). These systems are designed to be capable of deployment from buoy and ship platforms. Much of the previous longwave radiation sensor research and development has been devoted to observations from aircraft. Because our focus is on longwave observations from buoys and ships, different, and in most cases, more difficult constraints are presented (e.g., Katsaros 1990). The method we have selected for evaluating net longwave radiation measurements involves a hybrid technique in which the downwelling flux is measured directly using a pyrgeometer, while the upwelling radiation is modeled using sampled meteorological and sea surface variables (e.g., Katsaros 1990). Details concerning the theoretical and laboratory aspects of the present study are given in Dickey and Manov (1991), Manov (1991), Dickey et al. (1991), and Siegel and Dickey (1991).

In the following, a theory of the basic physics of thermopile-based pyrgeometers, which are used to directly measure downwelling longwave radiation, is summarized. The calibration and testing of pyrgeometers for our application are described. Examples of determinations of incoming longwave heat flux from surface buoy observations in four different oceanic regions are also presented. Finally, a method for the determination of net longwave radiation and its expected errors are given.

2. Theory of operation of a thermopile-based pyrgeometer

A pyrgeometer is similar to a pyranometer in that the voltage output of a thermopile is related to incident radiation (e.g., see reviews by Hinzpeter 1980; Katsaros 1990). However, a pyrgeometer utilizes a filter that ideally reflects downwelling shortwave radiation and transmits downwelling longwave radiation. The governing equation for downwelling longwave radiation LW$\downarrow$ for an ideal pyrgeometer is

$$\mathrm{LW}\downarrow = \frac{E}{\eta} + \epsilon_p \sigma T_p^4, \tag{2}$$

where E is the thermopile output voltage (μV), η is the sensitivity of the instrument [μV (W m^{-2})$^{-1}$], ϵ_p is the emissivity of the thermopile sensor plate, σ is the Stefan–Boltzmann constant (5.67×10^{-8} W m^{-2} K^{-4}), and T_p is the temperature (K) of the thermopile sensor plate (hot junction). The thermopile output voltage is given by

$$E = n\alpha(T_p - T_c), \tag{3}$$

where n is the number of thermopile junctions, α is the thermocouple sensitivity, and T_c is the temperature of the thermopile body or thermopile cold junction. For a working pyrgeometer, several complicating factors must be considered. Therefore, we summarize relationships based on first principles in order to minimize biases and errors in the determination of downwelled longwave radiation.

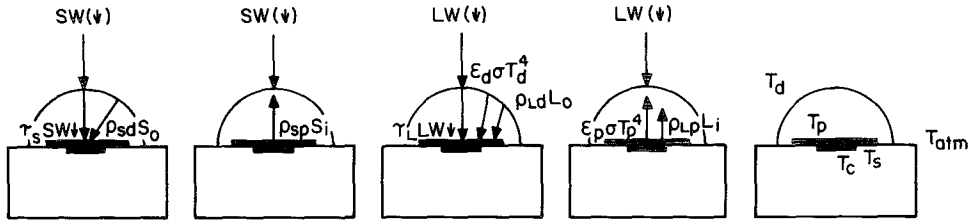

FIG. 1. Illustration of heat flux budget components of the pyrgeometer thermopile surface (sensor plate). Definitions are given in the text.

Eppley Laboratory pyrgeometers (Eppley Laboratory 1971, 1989) have been used for longwave radiation measurements by many researchers (e.g., Albrecht et al. 1974; Albrecht and Cox 1977; Weiss 1981; Bradley and Gibson 1982; Lind et al. 1984; see review by Katsaros 1990). The basic pyrgeometer unit selected for the present study is the stock (meaning unmodified version as obtained from the manufacturer) Eppley Laboratory model precision infrared radiometer (PIR) (see Eppley Laboratory 1989). A modified version of this pyrgeometer that employs a different thermopile, the Meteorological Research Flight Facility (MRF) thermopile developed by Foot (1986), was also used for this study.

The stock Eppley pyrgeometer consists of a thermopile enveloped by a hemisphere coated on the inside with silicon. It senses energy in the waveband between 4 and 50 μm and is intended to transmit no radiation with wavelengths less than 3.6 μm. The manufacturer's instrument characteristics are given in Table 1. Previous calibrations of the stock Eppley pyrgeometer have been described by Albrecht and Cox (1977) and its performance has been evaluated by several authors (e.g., Weiss 1981; Bradley and Gibson 1982; Ryznar and Weber 1982; Smith et al. 1988) who have primarily deployed it from aircraft.

The ability of the Eppley pyrgeometer to measure incident longwave radiation depends fundamentally on the heat budget of the sensor itself. A theory of operation has been presented by Campbell et al. (1978). Our work utilizes a similar theoretical development. A brief summary follows [details may be found in Dickey and Manov (1991)]. First, it is necessary to evaluate the energy flux budget (steady-state and equilibrium conditions are assumed) at the thermopile surface (see Fig. 1), or

$$S_i - S_o + L_i - L_o - H = 0, \tag{4}$$

where S_i and S_o are the incoming and outgoing shortwave (e.g., 0.3–3.0 μm) energy fluxes at the plate surface, L_i and L_o are the incoming and outgoing longwave energy fluxes at the plate, and H is the sum of the conductive and convective heat fluxes between the plate sensor and the cold junction and the flux between the plate and the dome. The various fluxes are illustrated in Fig. 1. After manipulation of the various balances, downwelling longwave radiation may be expressed as

$$\mathrm{LW}\downarrow = \frac{H}{\tau_L(1-\rho_{Lp})} + \frac{\epsilon_p(1-\rho_{Ld})\sigma T_p^4}{\tau_L(1-\rho_{Lp})} - \frac{\epsilon_d\sigma T_d^4}{\tau_L} - \frac{\tau_s(1-\rho_{sp})\mathrm{SW}\downarrow}{\tau_L(1-\rho_{Lp})}, \tag{5}$$

where τ_L is the longwave transmissivity of the dome, ρ_{Lp} is the longwave reflectivity of the plate, ϵ_p is the

TABLE 1. Instrument characteristics of the Eppley precision infrared radiometer (model PIR) as indicated by the manufacturer.

Sensitivity	~5 μV (W m^{-2})$^{-1}$
Impedance	~700 Ω
Temperature dependence	±2% for −20° to 40°C (nominal)
Linearity	±1% for 0–700 W m^{-2}
Response time	2 s (1/e signal)
Cosine response	better than 5% from normalization, insignificant for a diffuse source
Orientation	no effect on performance
Mechanical vibration	capable of withstanding up to 20 g's
Calibration	blackbody reference

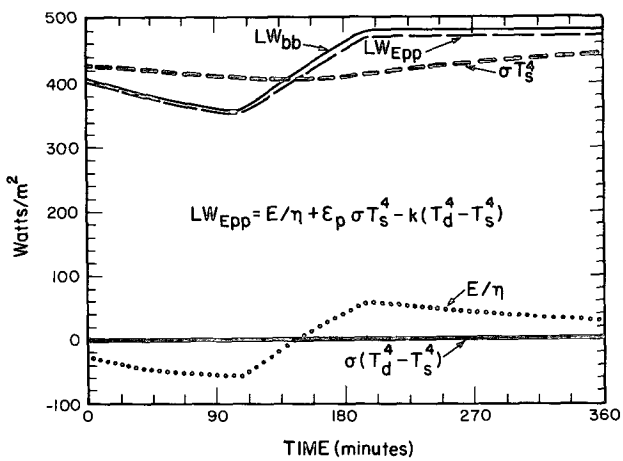

FIG. 2. Contributions of terms using the Albrecht and Cox (1977) formula for the calculation of longwave radiation in the calibration bath.

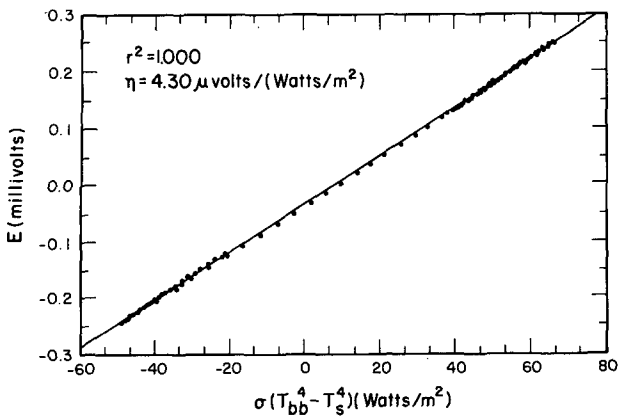

FIG. 3. Determination of sensitivity η using the Albrecht and Cox (1977) formula.

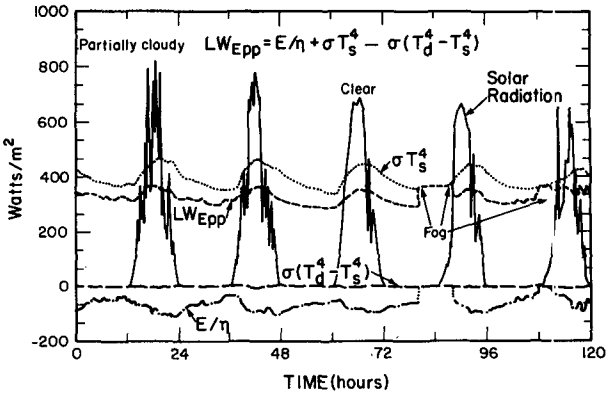

FIG. 5. Five-day time series of data illustrating contributions of terms to total longwave radiation for the Eppley pyrgeometer.

plate emissivity, ρ_{Ld} is the longwave reflectivity of the dome, ϵ_d is the longwave emissivity of the dome, T_d is the dome temperature, τ_s is the shortwave transmissivity of the dome, ρ_{sp} is the shortwave reflectivity of the dome, and SW$\downarrow$ is the downwelling shortwave irradiance incident on the dome.

It is useful to do a Taylor series expansion for T_p in terms of T_c or $T_p^4 = T_c^4 + 4T_c^3\delta + \cdots$, where $\delta = T_p - T_c$. Only the first two terms of the expansion are retained as $\delta/T_c \ll 1$ (as $\delta \sim 0.5$–1.0 K and $T_c \sim 280$–300 K). The output voltage E of the thermopile is given by Eq. (3) and is thus proportional to δ as is H (e.g., Albrecht et al. 1974). Using this information, Eq. (5) can be rewritten as

$$\mathrm{LW}\downarrow = E(c_1 + c_2T_c^3) + \frac{\epsilon_p(1-\rho_{Ld})\sigma T_c^4}{\tau_L(1-\rho_{Lp})} - \frac{\epsilon_d\sigma T_d^4}{\tau_L} - \frac{\tau_s(1-\rho_{sp})\mathrm{SW}\downarrow}{\tau_L(1-\rho_{Lp})}, \quad (6)$$

where constants c_1 and c_2 are determined from calibration. The thermopile cold junction temperature cannot be measured directly; however, the difference between this temperature and that measured in close proximity to the cold junction, T_s, or $T_c - T_s$, is assumed to be quite small because of the proximity of the cold junction with the thermistor measuring T_s and the high thermal conduction of the separating material. Therefore, we take $T_c = T_s$, and write Eq. (6) as

$$\mathrm{LW}\downarrow = \frac{E}{\eta} + k_1\sigma T_s^4 - k_2\sigma T_d^4 - k_3\mathrm{SW}\downarrow, \quad (7)$$

where the instrument sensitivity is defined as

$$\eta = (c_1 + c_2T_s^3)^{-1}$$

and where

$$k_1 = \frac{\epsilon_p(1-\rho_{Ld})}{\tau_L(1-\rho_{Lp})}, \quad k_2 = \frac{\epsilon_d}{\tau_L}, \quad \text{and} \quad k_3 = \frac{\tau_s(1-\rho_{sp})}{\tau_L(1-\rho_{Lp})}.$$

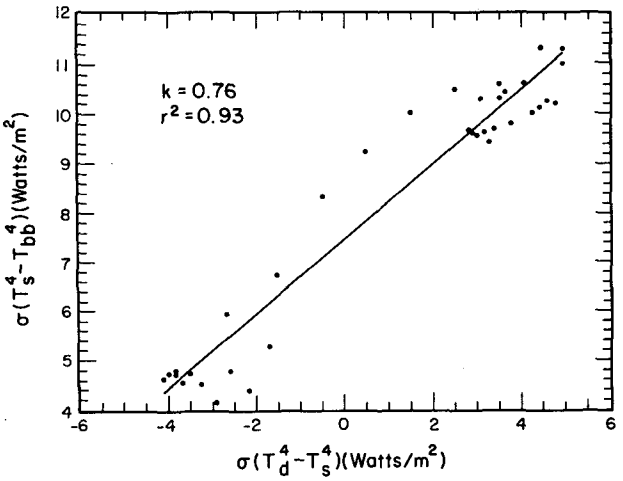

FIG. 4. Calculation of k using the Albrecht and Cox (1977) method.

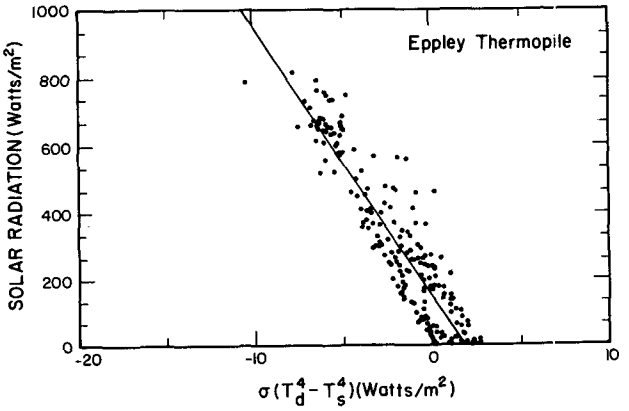

FIG. 6. Relation between solar radiation and heat flux induced by difference in dome and body temperatures.

It is possible to estimate values for several parameters in Eq. (6). The plate emissivity ϵ_p is 0.98 ± 0.01 (e.g., Campbell et al. 1978), the longwave emissivity of the dome ϵ_d is 0.3 ± 0.1 (e.g., Alados-Arboledas et al. 1988), the longwave and shortwave reflectivities of the plate, ρ_{Lp} and ρ_{sp}, are 0.02 ± 0.01 (e.g., Campbell et al. 1978), the dome reflectivity ρ_{Ld} is computed to be 0.43 ± 0.1 using the relation $\rho_{Ld} = 1 - \epsilon_d - \tau_L$ with the value of $\tau_L = 0.27 \pm 0.01$ being obtained from the measured transmission spectrum of the dome, and the shortwave transmissivity, $\tau_s = 0.0097 \pm 0.005$, is determined using the dome transmissivity value and the relationship between longwave and shortwave radiation obtained by Alados-Arboledas et al. (1988) and our value of τ_L. Using these values, $k_1 = 2.11 \pm 0.75$, $k_2 = 1.11 \pm 0.50$, and $k_3 = 0.036 \pm 0.013$. Then, Eq. (7) may be written as

$$\mathrm{LW}\downarrow = \frac{E}{\eta} + \sigma T_s^4 - 1.11\sigma(T_d^4 - T_s^4) - 0.036\mathrm{SW}\downarrow. \tag{8}$$

It is important to note that for a given pyrgeometer the only calibration parameter is η, which is also a weak function of T_s. Unfortunately, the uncertainties associated with the estimates of physical constants k_1, k_2, and k_3 are quite large. Further, these constants may vary between individual pyrgeometers (e.g., batch to batch differences in silicon domes). It is worth noting that Eq. (8) would revert to the form of the equation for an ideal pyrgeometer [Eq. (2)] if the dome and the thermopile cold junction (or sink) temperature were identical and if the shortwave radiation were completely reflected from the dome. The spectral transmissivity of the Eppley silicon dome and interference filter was measured here at the University of Southern California using an IBM System 9000 IR Spectraphotometer. Our calculations indicate a maximum value of radiation directly transmitted by the dome of less than 3%–4% shortwave (solar radiation). Similar results are reported by Alados-Aboledas et al. (1988) for an empirically derived dome correction factor.

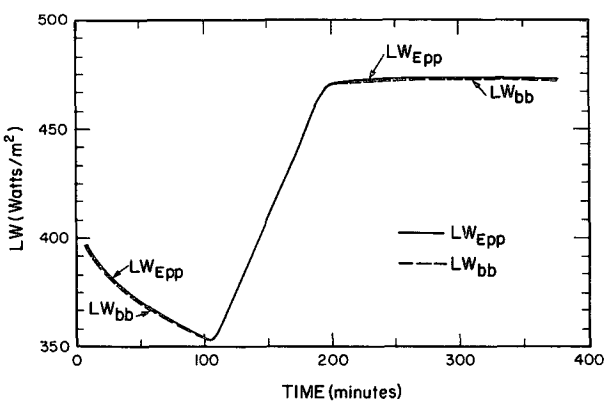

FIG. 7. Measured vs calculated longwave radiation using Eq. (12) for the Eppley thermopile.

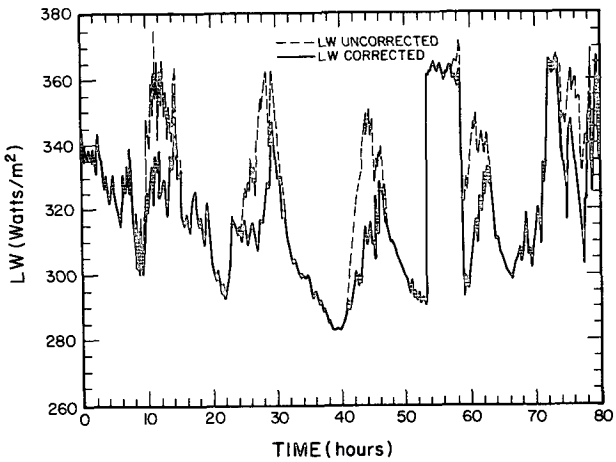

FIG. 8. Measured longwave illustrating the uncorrected longwave and the measured longwave corrected using Eq. (11).

TABLE 2. Calibration histories of the Eppley PIRs used in the experiments. Calibration (sensitivity) values chosen for use in converting the recorded output of the sensors to units of watts per square meter are indicated by an asterisk. Calibration data for one other PIR with a similar length history is included for comparison.

Eppley PIR SN	Calibration date	Calibration η [μV (W m^{-2})$^{-1}$]	Experiment
27026	22 Jun 1988	4.14*	pre-PreSubduction
	21 Aug 1989	4.03	post-PreSubduction
	7 Dec 1990	3.99	
	8 Jun 1992	4.06	
27027	22 Jun 1988	3.94*	pre-PreSubduction
	21 Aug 1989	4.11	post-PreSubduction
	7 Dec 1991	3.94*	pre-Subduction
	8 Jun 1992	4.04	post-Subduction
27185	21 Jul 1988	4.02*	pre-ERICA
	4 May 1989	4.37	post-ERICA
	7 Dec 1990	4.22	
27186	21 Jul 1988	3.98*	pre-ERICA
	4 May 1989	4.23	post-ERICA
	7 Dec 1990	4.06	
27364	9 Nov 1988	3.99	
	7 Dec 1990	4.07*	pre-MLML
	6 Nov 1991	3.73	first post-MLML
	11 Feb 1992	3.98	second post-MLML
27363	9 Nov 1988	3.61	
	7 Dec 1990	3.63	
	6 Nov 1991	3.53	
	11 Feb 1992	3.59	
27237	20 Sep 1988	3.77	
	28 Jun 1990	3.87	
	7 Dec 1990	3.91*	pre-MLML
	6 Nov 1991	3.57	first post-MLML
	11 Feb 1992	3.78	second post-MLML

TABLE 3. Basic statistics (mean, maximum, minimum, and standard deviation) of the longwave time series from both sensors on each buoy and of the time series of the differences between the two sensors on the same buoy.

Experiment/PIR	Mean (W m^{-2})	Max (W m^{-2})	Min (W m^{-2})	σ_{LW} (W m^{-2})
Presubduction				
V 704, PIR 27027	367.5	462.9	264.7	39.6
V 706, PIR 27026	445.4	517.7	312.1	36.4
$LW_{706} - LW_{704}$	77.9	140.4	−33.7	13.4
ERICA				
V 161, PIR 27186	293.7	394.8	199.5	35.9
V 707, PIR 27185	284.7	387.4	190.9	36.7
$LW_{707} - LW_{161}$	−9.0	61.3	−47.6	12.3
MLML				
V 706, PIR 27237	332.0	386.6	200.5	31.2
V 184, PIR 27364	330.2	380.2	231.3	30.4
$LW_{184} - LW_{706}$	−1.7	159.5	−20.4	12.2
Subduction				
V 704, PIR 27027	379.4	441.0	312.5	25.6
IMET	374.5	430.6	261.8	26.7
$LW_{IMET} - LW_{704}$	−4.9	32.3	−114.6	11.0

Finally, the formulation by Albrecht and Cox (1977) for the downwelling longwave flux measured by a pyrgeometer has been used by many investigators. It is given by

$$LW\downarrow = \frac{E}{\eta} + \epsilon_p \sigma T_s^4 - k\sigma(T_d^4 - T_s^4). \qquad (9)$$

Although our formulation appears quite similar to that of Albrecht and Cox (1977) and Albrecht et al. (1974), there are in fact significant differences. First, they assume that the shortwave radiation term is negligible whereas we do not. Foot (1986) argues that Eppley domes manufactured prior to 1985 effectively block shortwave radiation. However, for the more recently manufactured pyrgeometers used here, omission of the shortwave term can contribute an overestimate of over 30 W m^{-2} for shortwave values of 1000 W m^{-2}. Secondly, the last term in Eq. (9) is different from our analogous sum of terms [second and third on right-hand side of Eq. (8)]. Another important aspect concerns the interpretation of the variability of the parameter k. We do not take this as a free calibration parameter.

3. Testing and calibration

Instrument errors for Eppley pyrgeometers have been reported to the extent that only measurements made under special conditions, usually at night, have been considered valid by many investigators (e.g., Enz et al. 1975; Weiss 1981; Bradley and Gibson 1982; Brogniez et al. 1986). Improvements in the use of Eppley-type instruments tend to involve empirically derived correction factors (Brogniez et al. 1986; Foot 1986; Smith et al. 1988). These efforts have been directed almost exclusively toward improvements in longwave pyrgeometer performance in aircraft operations (well-ventilated conditions). Calibration techniques and correction factors derived for aircraft operations are not necessarily appropriate for obtaining accurate longwave measurements from surface-based (buoy and ship) pyrgeometers.

Three different basic pyrgeometers were considered. A standard Eppley Laboratory thermopile mounted on an Eppley body housing of bronze was compared with a specially configured thermopile designed at the Meteorological Research Flight Facility (MRF), Farnborough,

TABLE 4. Summary of estimates of error associated with calibration uncertainty and summary of mean observed difference between two longwave sensors on the same buoy. The mean observed LW, the mean sensitivity of the sensors from all its calibrations, the standard deviation of the sensitivity values (σ_{sens}), the estimated calibration error, the percentage that error is of the mean, and the mean observed difference are given except where a new sensor was used and there is no prior history of calibrations.

Experiment	Mean LW (W m^{-2})	Mean sensitivity η [μV (W m^{-2})$^{-1}$]	σ_{sens} [μV (W m^{-2})$^{-1}$]	Estimated calibration error (W m^{-2})	Percentage of mean (%)	Mean observed difference (W m^{-2})/(%)
PreSubduction						
V 704, PIR 27027	367.6	4.008	0.072	6.6	1.8	77.9/21.2
V 706, PIR 27026	445.5	4.055	0.055	6.0	1.4	
ERICA						
V 161, PIR 27186	293.7	4.090	0.104	7.5	2.5	−9.0/3.1
V 707, PIR 27185	284.7	4.203	0.143	9.7	3.4	
MLML						
V 706, PIR 27237	332.0	3.789	0.118	10.3	3.0	1.7/0.6
V 184, PIR 27364	330.0	3.943	0.128	10.7	3.2	
Subduction						
V 704, PIR 27027	379.4	4.008	0.072	6.8	1.8	4.9/1.3
IMET	374.5					

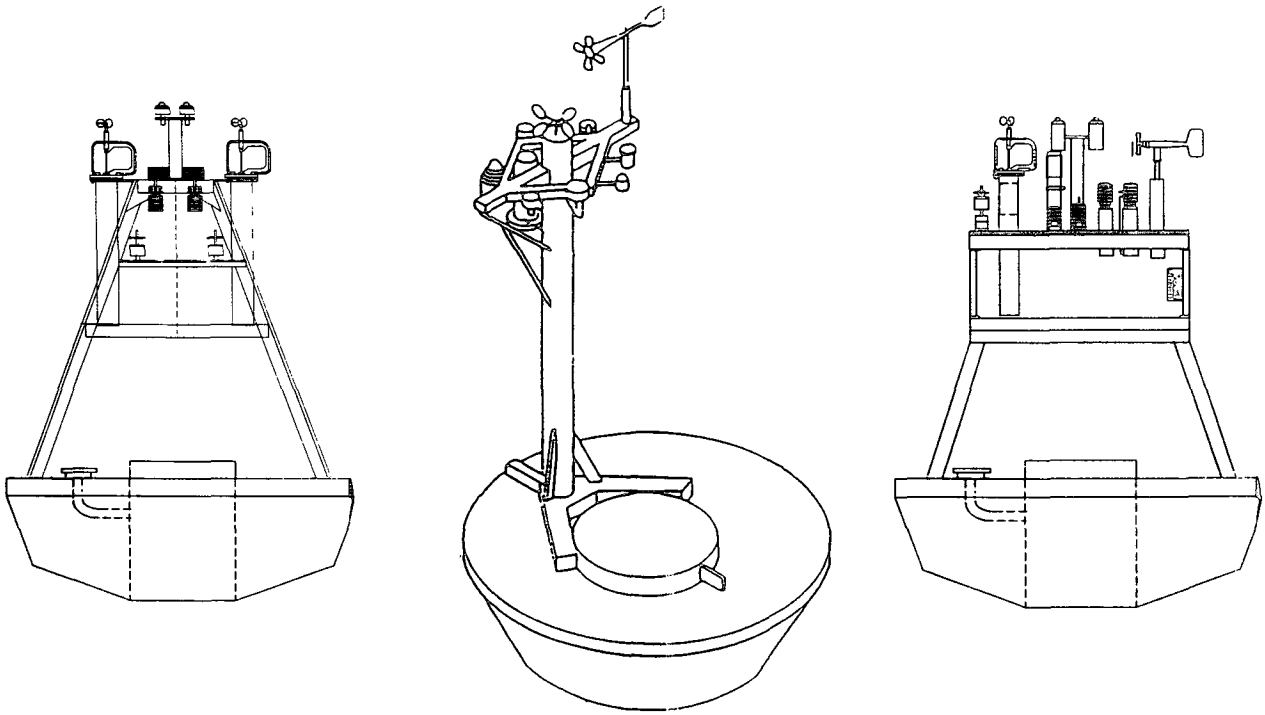

FIG. 9. Illustration of the 3-m-diameter discus buoys used in the field experiments. The three-legged superstructure (left) was used in PreSubduction and MLML. The single mast (center) was used in ERICA to minimize ice buildup, and the modified three-legged design (right) was used in Subduction. The PreSubduction, ERICA, and MLML buoys carried the sensors associated with two vector-averaging wind recorders (VAWRs), including incoming shortwave radiation, incoming longwave radiation, wind velocity, relative humidity, barometric pressure, air temperature, and sea surface temperature. The Subduction buoy carried one set of VAWR sensors and one set of IMET sensors.

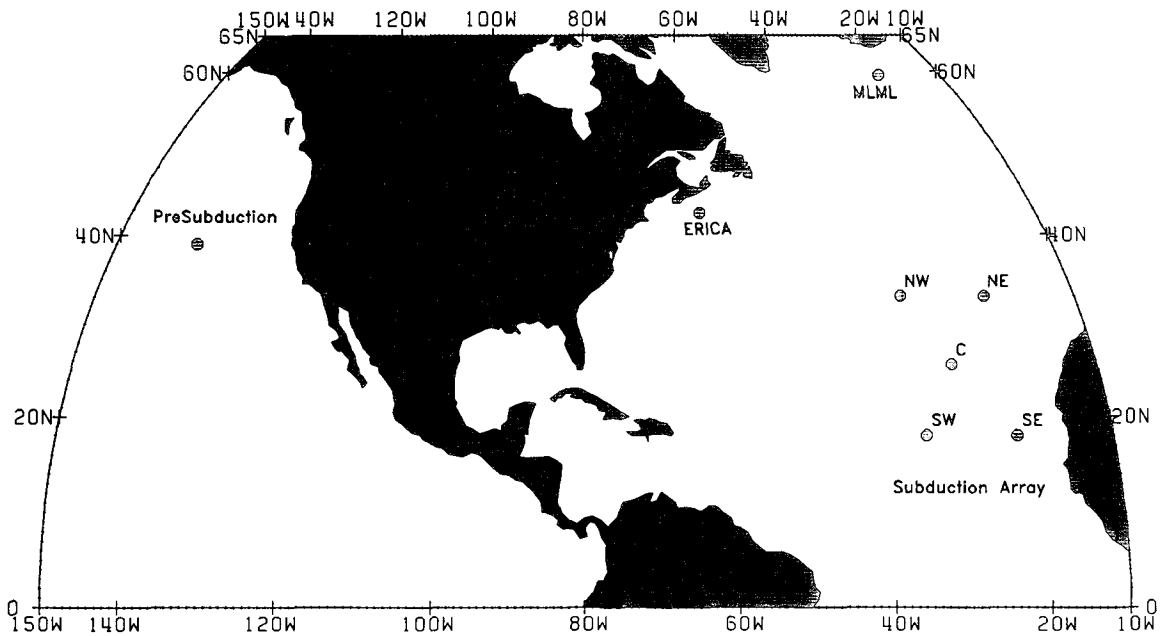

FIG. 10. Map showing the location of the PreSubduction, ERICA, MLML, and Subduction experiments.

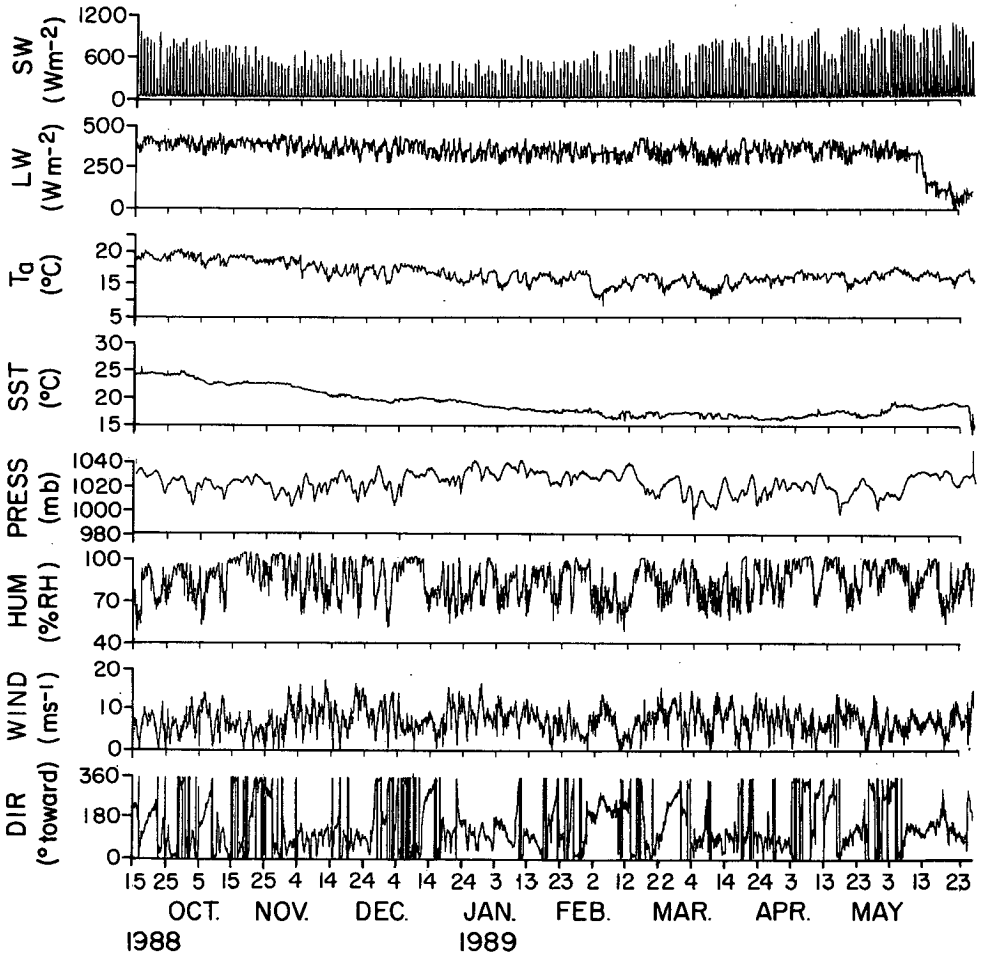

FIG. 11. Time series of meteorological variables and sea surface temperatures recorded by VAWR 704 on the PreSubduction buoy. From top to bottom: incoming shortwave radiation (W m^{-2}), incoming longwave radiation (W m^{-2}), air temperature (°C), sea surface temperature (°C), barometric pressure (mb), relative humidity (%), wind speed (m s^{-1}), and wind direction (degrees toward).

England (Foot 1986), and mounted on a similar body of aluminum. An additional comparison was made using the MRF thermopile on three bodies of equal dimensions made of aluminum, brass, and lead to examine thermal inertia effects. Details concerning the MRF testing are presented in Manov (1991).

The standard manufactured Eppley pyrgeometer (PIR) uses a thermistor–resistor network compensation circuit to apply a voltage proportional to the σT_c^4 term and a temperature-compensated thermopile that represents the term $E(c_1 + c_2 T_c^3)$ in Eq. (6). This circuit is not intended to correct for the temperature differential between the dome and the body. For all atmospheric temperatures, $c_1 \gg c_2 T_c^3$ and $E(c_1 + c_2 T_c^3)$ is typically three to four times smaller (in absolute value) than σT_c^4 (note T_c is set equal to T_s). The $\sigma(T_d^4 - T_c^4)$ term is small in comparison to LW↓. Consequently, errors in the electrically compensated thermopile output may not contribute significantly to errors in the measured irradiance value. Errors in the instrument equivalent of the σT_c^4 term, however, may be significant (Albrecht and Cox 1977). The Eppley temperature compensation circuit for σT_c^4 is generally not used for our work and T_s, T_d, and E are measured directly. It should be noted that the use of the compensation circuit imposes a limitation on the deployment period because of finite battery lifetime (see discussion of the PreSubduction experiment dataset of section 6). Thus, there is a significant advantage in omitting this circuit.

Two calibration methods are used by Eppley Laboratory (1989). For the first, the pyrgeometer is exposed to an ideal blackbody radiator with varying temperature. The second involves a comparison against a calibrated working standard pyrgeometer with a steady longwave source such as the cloudless night sky.

For the present work, a specially designed laboratory calibration facility and a terrestrial site were used for

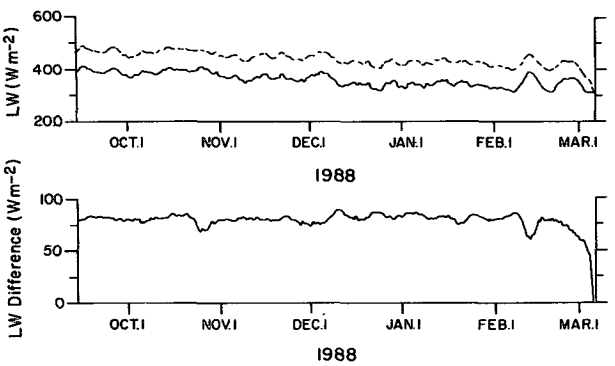

FIG. 12. Time series of incoming longwave radiation from the two Eppley PIRs deployed on the PreSubduction buoy. The data have been low-pass filtered (4-day boxcar); LW_{704} is the solid line, and LW_{706} is the dashed line. The time series of the difference of the two ($LW_{706} - LW_{704}$) is plotted below.

calibration and preliminary testing purposes. The laboratory work utilized a water bath (~200 L) with temperature controlled using regulated heating and chilling units. The temperature is measured with a precision thermometer to ±0.01 K. The pyrgeometers were placed in a copper dome painted black, which is built into the center bottom of the tank. This dome acts as the blackbody source with temperature T_{bb}, and the effective longwave radiation is given by $LW_{bb} = \epsilon_{bb}\sigma T_{bb}^4$ where the emissivity of the dome is ϵ_{bb} and the temperature is T_{bb}.

Calibrations were done by applying the commonly used formulation of Albrecht and Cox (1977). Taking $LW\downarrow = LW_{bb}$, Eq. (9) may then be written as

$$LW_{bb} = \epsilon_{bb}\sigma T_{bb}^4 = \frac{E}{\eta} + \epsilon_p \sigma T_s^4 - k\sigma(T_d^4 - T_s^4). \quad (10)$$

The temperature of the blackbody source (our temperature bath), is varied slowly and allowed to approach a steady-state condition. The values of ϵ_{bb} and ϵ_p are taken to be equal to 1. Near equilibrium, T_s is nearly equal to T_c, and T_d nearly equals T_s with only a small difference when compared to T_{bb}. These are the conditions that best describe the parameters for ground-based pyrgeometers and the ones most closely simulated by our thermal bath. As the bath temperature is varied until equilibrium is reached ($T_d = T_s$), Eq. (10) reduces to $E/\eta = \sigma(T_{bb}^4 - T_s^4)$. To determine the thermopile sensitivity η in Eq. (10), the instrument output E is plotted versus $\sigma(T_{bb}^4 - T_s^4)$ for values where $\sigma(T_d^4 - T_s^4)$ is very small or equal to zero. Contributions of the four terms in Eq. (10) are illustrated in Fig. 2 for a 6-h calibration run (here we take $k = 1$). The longwave radiation from the bath (LW_{bb}) and the measured longwave from the instrument (LW_{Epp}) are within about 10 W m^{-2} of each other. The determination of η is illustrated in Fig. 3. It should be possible to determine the value of k by plotting $\sigma(T_s^4 - T_{bb}^4)$ as a function of $\sigma(T_d^4 - T_s^4)$. In actual practice, however, the variations in T_d and T_s are dependent and the range is very small. A relatively poor fit to the curve is apparent in Fig. 4. It is apparent that k as defined in Eq. (10) is not constant and is highly specific to the particular configuration and calibration run. The measured value of this "dynamic k" is only applicable for restricted conditions of the atmosphere, which make this method inefficient for general use, particularly for earth surface applications.

4. Practical considerations for pyrgeometer measurements

A time series for a 5-day period of measured longwave radiation at a terrestrial site near Los Angeles using the Albrecht and Cox formula is shown in Fig. 5. Solar radiation is apparently an important source of error for the pyrgeometers used in this study. Using the Albrecht and Cox formula, our time series data show a nominal daytime correction [term $k\sigma(T_d^4 - T_s^4)$] of approximately 10 W m^{-2} (Fig. 6 for an Eppley thermopile). The value of the correction increases proportionately for any increase in k and the error resulting from the term is dependent on the accuracy of the determination of k.

The value of k is shown to be quite variable and difficult to measure. These difficulties are readily apparent in the studies of Weiss (1981), Brogniez et al. (1986), and Foot (1986) as well as our own. For near-equilibrium conditions, k is dependent upon the thermal time constants, rapidity of change in T_d, thermal inertia of the body, and initial absolute temperatures.

The results for thermal bath runs show a decreasing responsivity to longwave (and subsequently a smaller value of η) with an increasing heat capacity of the body (larger mass and thermal inertia). The slope for aluminum is 1.01, brass 1.04, and lead 1.08, indicative of the "nontracking" of T_s and T_{bb}. The value of η for the same thermopile decreases from 2.25 for aluminum to 2.17 for brass, and to 1.94 for lead. This result is expected as η is a function of T_c, which is dependent on T_s (thermistor is embedded in the material of the body). The values appear to be specific to the instrument configuration and are probably not relevant to other types of pyrgeometers. The comparative time series for field measurements (Fig. 5) illustrates a similar effect. For nighttime, the bodies of both aluminum and bronze show a similar temperature correlation with the MRF pyrgeometer body responding more closely to the atmospheric temperature and the responsivity of the aluminum housing being more ideal. Solar radiation increases the differences between the air temperature T_{air} and the temperature of the body T_s, which contributes to the error in both the thermopile voltage E and the σT_s^4 term.

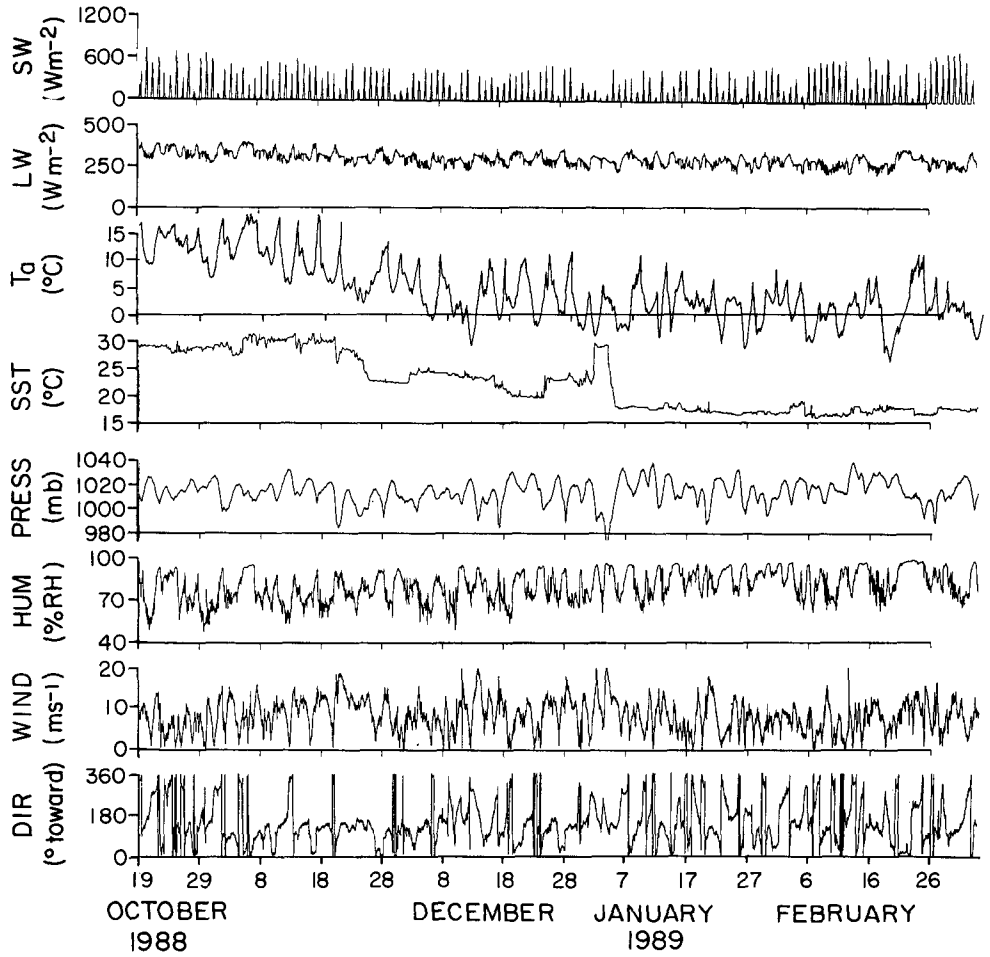

FIG. 13. Near-surface meteorological variability as recorded by the VAWR 161 on the ERICA surface buoy. From top to bottom: incoming shortwave radiation (W m^{-2}), incoming longwave radiation (W m^{-2}), air temperature (°C), sea surface temperature (°C), barometric pressure (mb), relative humidity (%), wind speed (m s^{-1}), and wind direction (degrees toward) are shown.

During field measurements, the body is heated primarily by solar radiation. There is a thermal lag between the body temperature and that of the atmosphere. The magnitude of the lag is affected by the absolute temperature difference and the effective conduction between the body and the atmosphere. As wind speed increases, the temperature differences decrease. The body temperature T_s is more closely related to the temperature difference between the body and the atmosphere than to the solar radiation effects. The absolute temperature differences between the dome T_d and the body T_s are also strong functions of solar radiation with a much smaller time lag due to the lower thermal inertia of the dome and increased ventilation effects on the differences in the dome and body temperatures. The dome and body respond much more rapidly and have less absolute difference in response to environmental changes than does the body. Additional details and test results are described in Manov (1991).

Next, we consider the method developed here for determining LW↓, which utilizes Eq. (8) or rewriting,

$$\mathrm{LW}\downarrow = \frac{E}{\eta} + 2.11\sigma T_c^4 - 1.11\sigma T_d^4 - 0.036\mathrm{SW}\downarrow. \quad (11)$$

By neglecting shortwave radiation effects, the calibration bath formulation becomes

$$\mathrm{LW}_{bb} = \epsilon_{bb}\sigma T_{bb}^4 = \frac{E}{\eta} + 2.11\sigma T_c^4 - 1.11\sigma T_d^4. \quad (12)$$

Assuming that the body thermistor T_s is an accurate measure of the cold junction temperature T_c and solving for η results in a value of 4.186 μV (W m^{-2})$^{-1}$ for an Eppley pyrgeometer and a value of 2.310 μV (W m^{-2})$^{-1}$ for an MRF pyrgeometer. The calculated and measured results using this method are shown in Fig. 7 and are within 2 W m^{-2} for the entire run. A 3-day time series of the uncorrected LW↓ and the LW↓

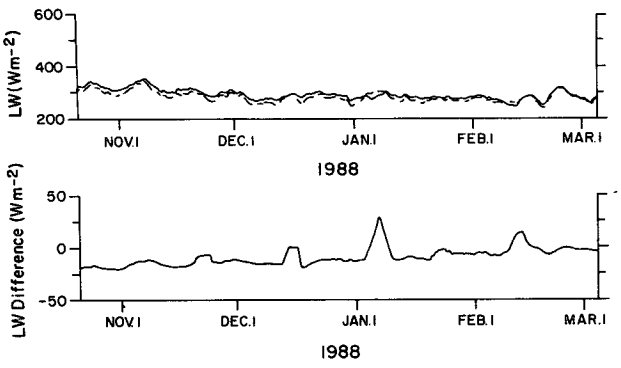

FIG. 14. Overplot of the two records of incoming longwave radiation obtained during ERICA; LW_{161} is the solid line and LW_{707} is the dashed line. The time series of the difference of the two ($LW_{707} - LW_{161}$) is plotted below.

computed with the new method [Eq. (11)] are shown in Fig. 8. The relative improvement is apparent in the reduced daytime values (by approximately 20–40 W m^{-2}) especially during the broken cloud condition (first 24-h period). Broken cloud cover (see first peak in Fig. 8) seems to reduce the overall thermal heating of the body. The solar radiation effect is therefore limited or reduced by alternating periods of relatively rapid cooling and reradiation of body heat to the atmosphere. On a clear day, the effect is to gradually heat the body with respect to the atmosphere and then to slowly reradiate this thermal energy back to the atmosphere, resulting in a gradual increase and then a gradual decrease in measured longwave radiation (second and third peaks in Fig. 8). This result suggests that the new method is preferable for most environmental conditions.

At this point, we summarize our results with respect to the determination of LW↓ using pyrgeometers. Our formulation of LW↓ using pyrgeometer data is given by Eq. (6), but may be expressed for convenience in the form

$$\mathrm{LW}\downarrow = \underbrace{\frac{E}{\eta}}_{\text{(I)}} + \underbrace{\sigma T_s^4}_{\text{(II)}} - \underbrace{k\sigma(T_d^4 - T_s^4)}_{\text{(III)}} - \underbrace{K\mathrm{SW}\downarrow}_{\text{(IV)}}. \quad (13)$$

In general, the thermopile output, term I, contributes 0–100 W m^{-2} of the total longwave; the absolute body temperature, term II, contributes 200–400 W m^{-2}; the difference in dome and body temperatures, term III, contributes 0–40 W m^{-2}; and the shortwave, term IV, contributes 0–30 W m^{-2}.

5. Interfacing of longwave sensor to IMET system

The development of improved meteorological systems including data loggers and sensors is one of the primary objectives of the IMET program. Since these systems are to be deployed on buoys and ships, special design considerations are required. Detailed technical information concerning system data acquisition and control is given in Weller and Hosom (1989), Prada et al. (1990), Allsup (1990), and Prada (1990). A brief summary concerning the longwave sensor configuration and the data acquisition system follows.

For deployment on buoys and ships during WOCE, the Eppley housing weight was reduced for a gimballed mounting configuration (Crescenti et al. 1989a; MacWhorter and Weller 1991). The instrument has a smaller dome housing and an aluminum body consistent with our study, allowing T_s to track more closely the temperature of the atmosphere. The calculated longwave has been shown to correspond nearly exactly with the measured longwave from the modified Eppley pyrgeometer (see Manov 1991).

The ship data logger/controller is an NEC APC-IV personal computer and the buoy data logger/controller is a low-powered (0.5 W) version of this system. Optical disks are used for storage, and the system supports an Argos platform transmitter terminal (PTT) for data telemetry as well as flexible sampling–logging software. The suite of meteorological sensors (8) measure wind speed and direction, air and sea surface temperature, barometric pressure, relative humidity, downwelling shortwave and longwave radiation, and precipitation. Sensors besides those described here have been redesigned based on available standard meteorological sensors with the intent of reducing the errors associated with the determination of fluxes of momentum and heat fluxes at the air–sea interface. These include pyranometers (Crescenti et al. 1989b), air and sea surface temperature sensors (Crescenti et al. 1989c), precipitation sensors (Crescenti and Weller 1989; Hinton 1990), humidity sensors (Crescenti and Payne 1991; Crescenti et al. 1990; Crescenti et al. 1991a; Hosom et al. 1991), and barometric pressure (Payne et al. 1989). In addition, reliability and robustness as well as economy have been important factors in the developmental efforts.

Each sensor is interfaced to a microprocessor-based module that performs sampling tasks, voltage to engineering unit conversions, and digital data transmission to the data logger/controller through either an RS-485 link for ships or an RS-232 link for buoys. For our particular work, a prototype longwave sensor has been interfaced to the Woods Hole Oceanographic Institution IMET system. The pyrgeometer housing and the BASICON module have been combined with a gimbal mounting for testing of the IMET system onboard buoys and on ships. The computation of fluxes are done utilizing the best available algorithms. The raw data, taken at rates as rapidly as once per minute (for one year), are stored and averaged (for periods of several hours). Variable and flux data may be telemetered using the Argos satellite communications link.

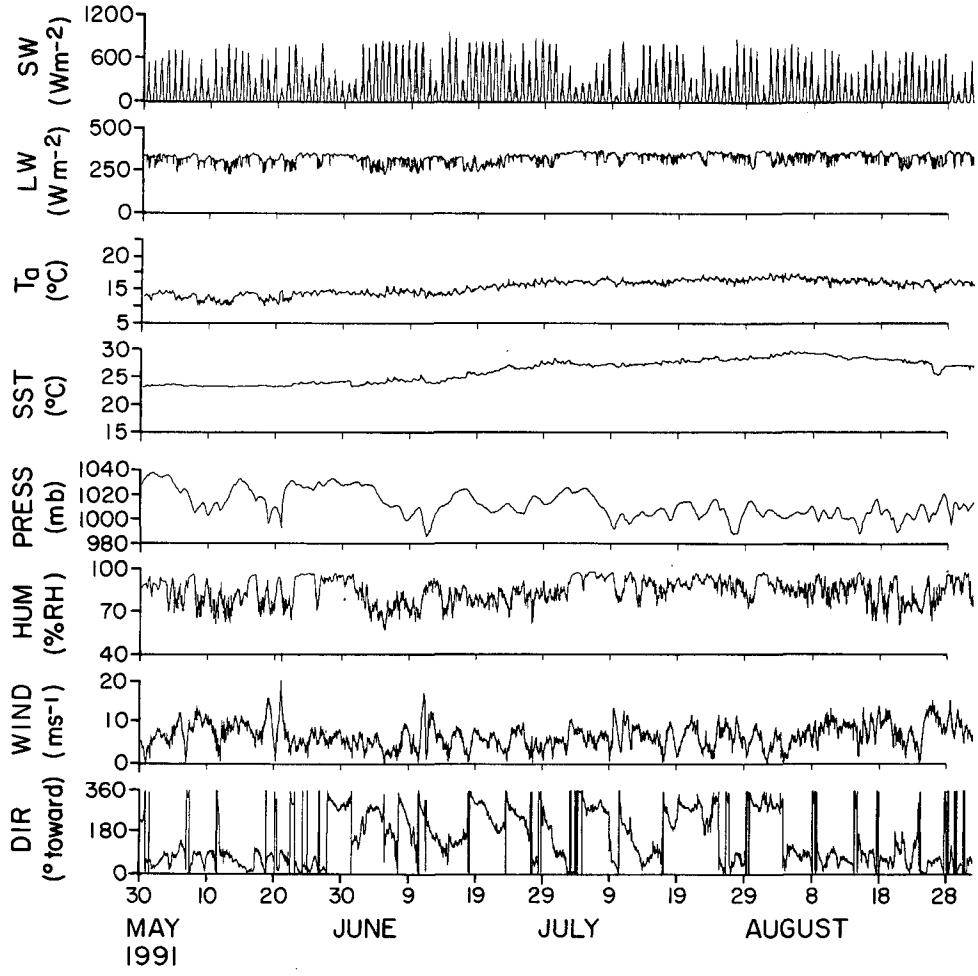

FIG. 15. Meteorological variability observed by VAWR 184 on the MLML mooring. From top to bottom: incoming shortwave radiation (W m^{-2}), incoming longwave radiation (W m^{-2}), air temperature (°C), sea surface temperature (°C), barometric pressure (mb), relative humidity (%), wind speed (m s^{-1}), and wind direction (degrees toward) are shown.

6. Field measurements of downwelling radiation using Eppley and IMET sensors

Four deployments of longwave radiation sensors were chosen to examine the accuracy of incoming longwave radiation measurements made at sea. Calibration histories, basic statistics, and error estimates are given in Tables 2, 3, and 4. For each deployment, two longwave sensors were mounted at the same height and with a clear field of view on the same 3-m-diameter discus buoy (Fig. 9). Two stock Eppley PIR sensors provided data in three of the experiments; in the fourth an IMET longwave sensor was deployed along with a stock Eppley PIR. The differences between the records of the two longwave sensors were examined for each experiment. Following is a summary of results of these experiments along with descriptions of calibration and radiometric difference uncertainties.

a. PreSubduction experiment

The first experiment was the PreSubduction experiment, where a 3-m-diameter discus buoy was deployed

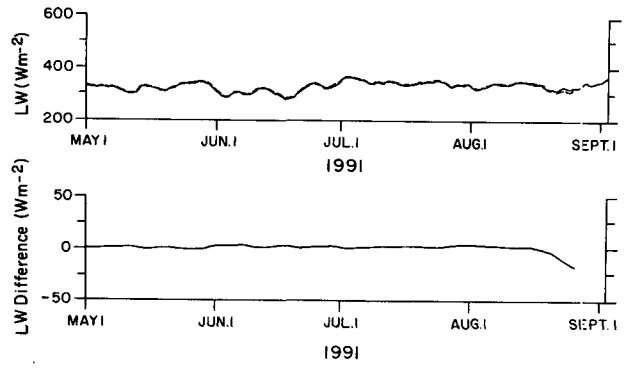

FIG. 16. Overplot of the two incoming longwave radiation time series recorded by the two VAWRs on the MLML buoy; LW_{706} is the solid line and LW_{184} is the dashed line. The time series of the difference of the two ($LW_{184} - LW_{706}$) is plotted below.

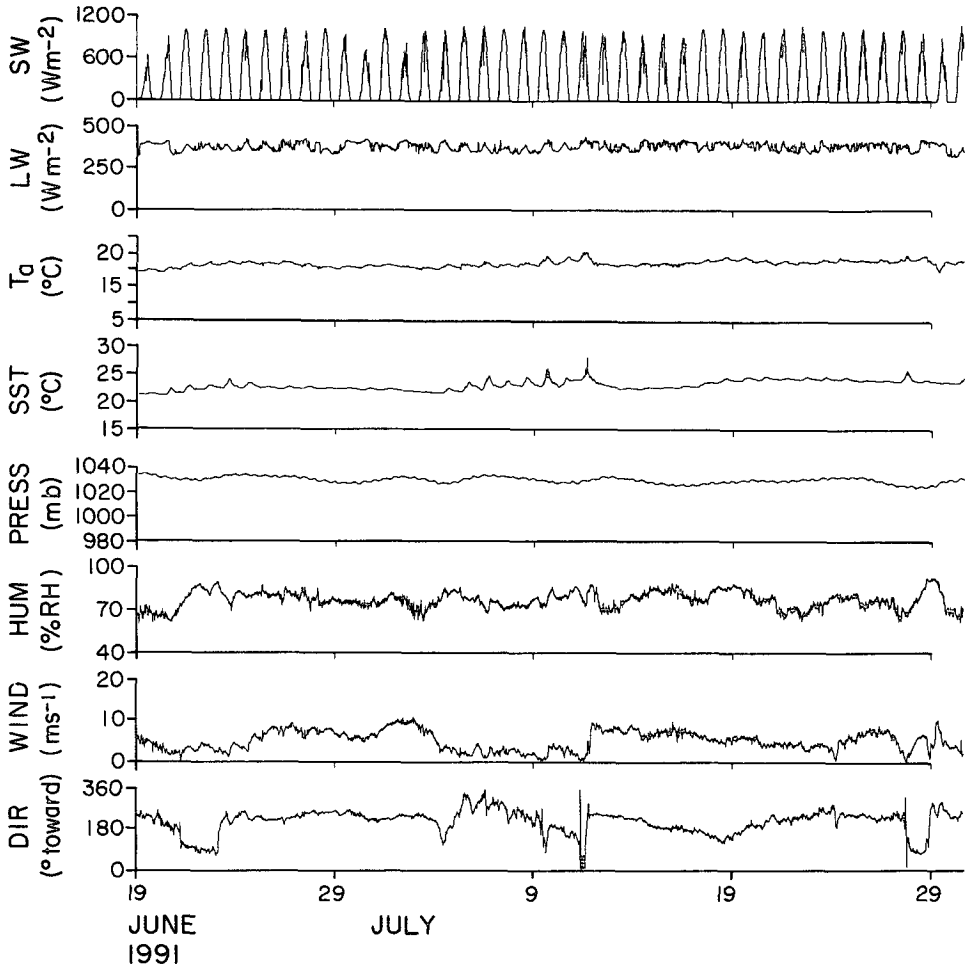

FIG. 17. Meteorological variability observed by VAWR 704 on the Subduction northeast mooring. From top to bottom: incoming shortwave radiation (W m^{-2}), incoming longwave radiation (W m^{-2}), air temperature (°C), sea surface temperature (°C), barometric pressure (mb), relative humidity (%), wind speed (m s^{-1}), and wind direction (degrees toward) are shown.

in the eastern North Pacific at 39°60'N, 137°01'W (Fig. 10) from 15 September 1988 to 29 May 1989 (257 days). Two vector-averaging wind recorders (VAWRs) (Weller et al. 1990; Dean and Beardsley 1988; Payne 1974) were mounted on the buoy. Each recorded wind velocity, barometric pressure, air temperature, sea surface temperature, relative humidity, incoming shortwave radiation, and incoming longwave radiation (Fig. 11). Data were recorded on magnetic tape every 900 s (15 min). The stock Eppley PIR sensors had amplifiers located directly below the sensors. The amplified voltages were digitized by the VAWR. For the duration of the 15-min sample interval, the signal-conditioning electronics associated with the longwave sensor convert the amplified voltage to a signal whose frequency is proportional to the voltage and the digitization is carried out by counting over the interval to determine the frequency. Calibration of the signal-conditioning electronics in conjunction with calibration of the Eppley PIR provides the means to convert the recorded frequency to incoming radiation.

Problems experienced by one of the two VAWRs (PIN SN 27027) late in the experiment led to questions about the accuracy of its data, especially after late March 1989. As mentioned earlier, the stock Eppley PIR sensor uses a 1.35-V battery as a reference in its internal temperature compensation circuitry. By the end of the deployment, this battery was exhausted. The abrupt change in measured incoming longwave radiation (the notation LW_x will be used to denote the observed longwave radiation from VAWR x) in early February 1989 (Fig. 12) is believed to correspond to the failure of this battery. Prior to this, 177 days of data exist from both longwave sensors and have been analyzed.

VAWRs SN 704 and 706 were used in Pre-Subduction. The basic statistics of the longwave time series data are summarized in Table 3. The correlation

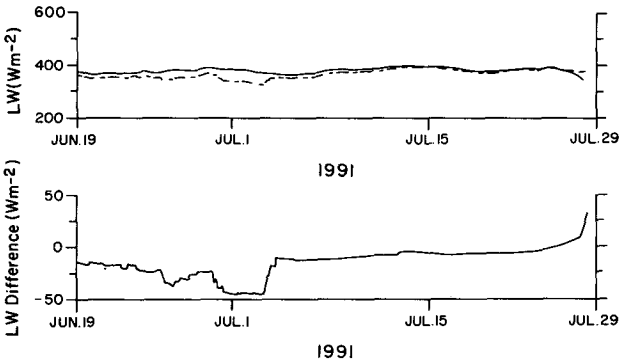

FIG. 18. Overplot of the two records of incoming longwave radiation obtained during Subduction; LW_{704} is the solid line and LW_{IMET} is the dashed line. The time series of the difference of the two ($LW_{IMET} - LW_{704}$) is plotted below.

coefficient between LW_{706} and LW_{704} was 0.94. The two PIRs were calibrated by Eppley Laboratory before and after the deployment. The calibration sensitivity values for PIR SN 27027 used on V 704 increased by 4.3%; the calibration sensitivity value for PIR SN 27026 decreased by 2.7%. The record from sensor LW_{704} was judged to be in error because of its unrealistically high mean value. The high correlation between the two records, similar standard deviations, and similar ranges between maximum and minimum observed values suggest that LW_{704} was biased high by 77.9 W m^{-2}. The calibration of the PIR sensor was repeatable, and the source of this bias is thought to be the VAWR electronics.

b. *ERICA*

The second experiment was ERICA [Experiment on Rapidly Intensifying Cyclones over the Atlantic; see Hadlock and Kreitzberg (1988)], conducted from 18 October 1988 to 7 March 1989 off the coast of Maine. In this experiment a 3-m discus buoy was deployed at 42°33′N, 61°14′W with two VAWRs (Fig. 10). For this experiment, a single mast was used on the buoy to minimize the surface area available for icing rather than the tripod used in the other deployments (Fig. 9). The sampling interval for the VAWRs was 450 s (7.5 min), and a 141-day time series of surface meteorology in a region characterized by the passage of winter storms was collected. These data include 141 common days of good longwave data from both instruments.

A series of storm events, characterized by cloudy skies, high winds, and air temperatures near freezing were observed and have been described by Crescenti and Weller (1992) (Fig. 13). Instrument and sensor performance was examined after the deployment (Crescenti et al. 1991b). Incoming longwave radiation had variations of up 150 W m^{-2} as low clouds associated with the storms entered and departed the site. The two VAWRs used in ERICA were numbers V 161 (with Eppley PIR SN 27186) and V 707 (Eppley PIR SN 27185). The Eppley PIRs were calibrated before and after the experiment (Table 2) with +6.3% and +8.7% changes in calibration sensitivity values, respectively. The precruise calibration sensitivity values were used to process the data (Fig. 14), and basic statistics are summarized in Table 3. A linear regression resulted in the relation $LW_{707} = 0.966LW_{161} + 1.11$ with a standard error of 12.24. The two records were in better agreement than the two obtained in the PreSubduction experiment.

c. *MLML experiment*

The third experiment was the Marine Light in the Mixed Layer (MLML) experiment, which had a 3-m discus buoy in place at 59°37′N, 20°58′W (Fig. 10) from 29 April to 6 September 1991. Two VAWRs (V 706 and V 184) were again deployed on the surface buoy, and the two Eppley PIRs (SN 27237 and SN 27364) obtained 112 days of good data in common. Sampling and digitization of the longwave radiation was done as it had been in PreSubduction and ERICA, and the basic sampling interval was again 900 s (15 min). The PIRs were calibrated before and after the experiment. The calibrations done immediately after the experiment were considered suspect, and a second set of postcruise calibrations was carried out. The data were processed using the precruise calibrations. Values from LW_{706} (PIR SN 27237) began to fall below those of LW_{184} on about 20 August 1991 and fell off abruptly in late August (Fig. 16). The initial modest and later abrupt decrease in the PIR output is attributed to the end of life of the battery in the internal circuitry of the PIR.

The location of the MLML mooring, just south of Iceland, is characterized by strong atmospheric forcing, with a number of storms and accompanying high winds (Fig. 15). The mooring was in place during late spring and summer, but peak winds were in excess of 20 m s^{-1} and on some days there was little incoming shortwave radiation. Incoming longwave ranged from 200 to 387 W m^{-2}, with a variation of up to 100 W m^{-2} associated with variation in cloud cover on timescales of hours to days. The correlation coefficient between the two records was 0.92. The mean value of the time series of the difference between the two records (Fig. 16) was low, 1.7 W m^{-2}. Other statistics are given in Table 3.

The calibrations from before the deployment were used for processing the MLML data. The initial postdeployment calibration sensitivity values were 8.7% (PIR SN 27237) and 8.4% (PIR SN 27364) lower than the predeployment calibrations. The changes in calibrations were judged to be too large by comparison to the change seen in other deployments, and the sensors were returned to Eppley Laboratory for another cali-

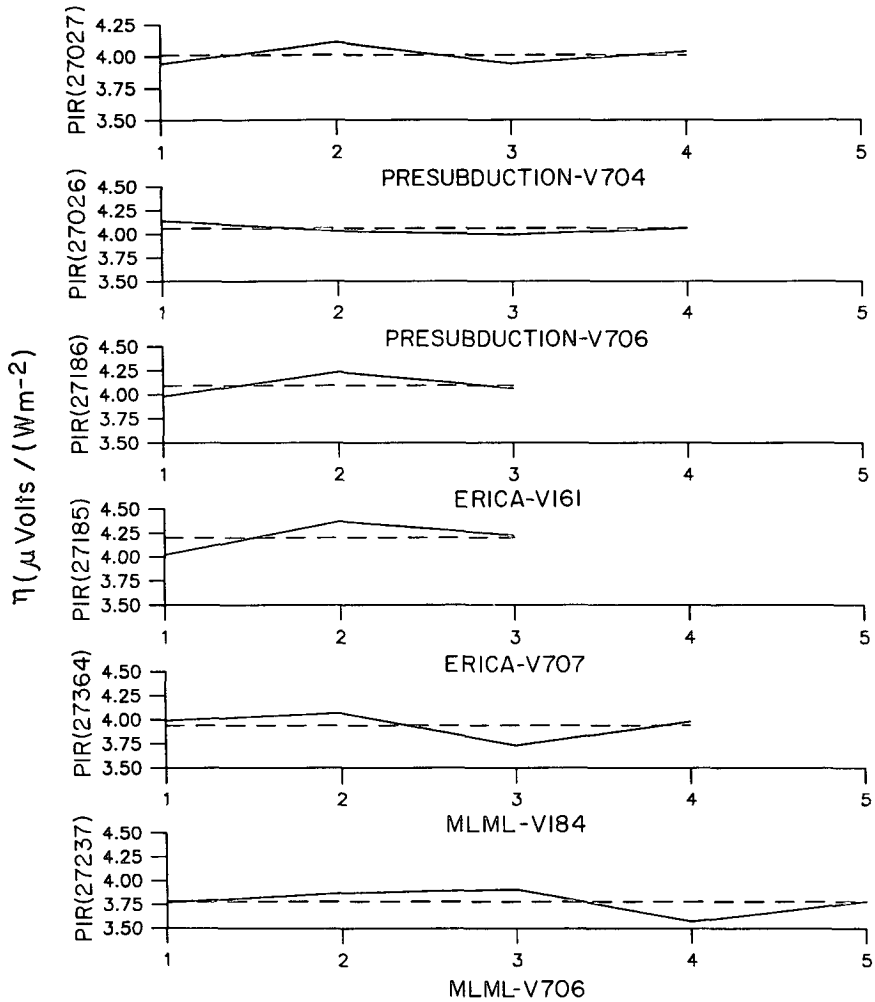

FIG. 19. Calibration histories of sensitivities η of various Eppley PIR sensors. Top two panels are for PreSubduction, the next two panels are for ERICA, and the lower two panels are for MLML. Ordinate axis is in units of microvolts per watts per square meter.

bration. The second postdeployment calibration was closer to the predeployment calibration, with 3.3% and 2.2% changes between the predeployment and new calibration sensitivity values, respectively, SN 27237 and SN 27364.

d. Subduction experiment

The most recent experiment was the Subduction experiment, which placed an array of five surface buoys in the eastern North Atlantic in the summer of 1991 (Fig. 10). The buoy in the northeastern corner of the array (NE) had an Eppley PIR attached to a VAWR and a modified Eppley PIR attached to an IMET instrument. The full suite of meteorological measurements is shown in Fig. 17. The two instruments gave 41 days of good longwave data in common, from 19 June to late July 1991 (Fig. 18). The VAWR longwave radiation was sampled as it had been in previous experiments, with a record interval of 900 s (15 min). The IMET instrument had a record interval of 60 s (1 min), and the longwave radiation recorded was the average of the incoming longwave radiation measured over that minute. To compare the records, the IMET data were further averaged to produce a dataset with a 15-min sampling interval.

The standard PIR was recalibrated after the deployment; the change in the calibration sensitivity value was 2.5%. The IMET instrument has not yet been recalibrated. The incoming longwave records from the two sensors were close. The mean of the difference time series (Fig. 18) was 4.9 W m^{-2}, and the standard deviation was 11.0 W m^{-2}. The correlation coefficient was 0.91. Other statistics are given in Table 3.

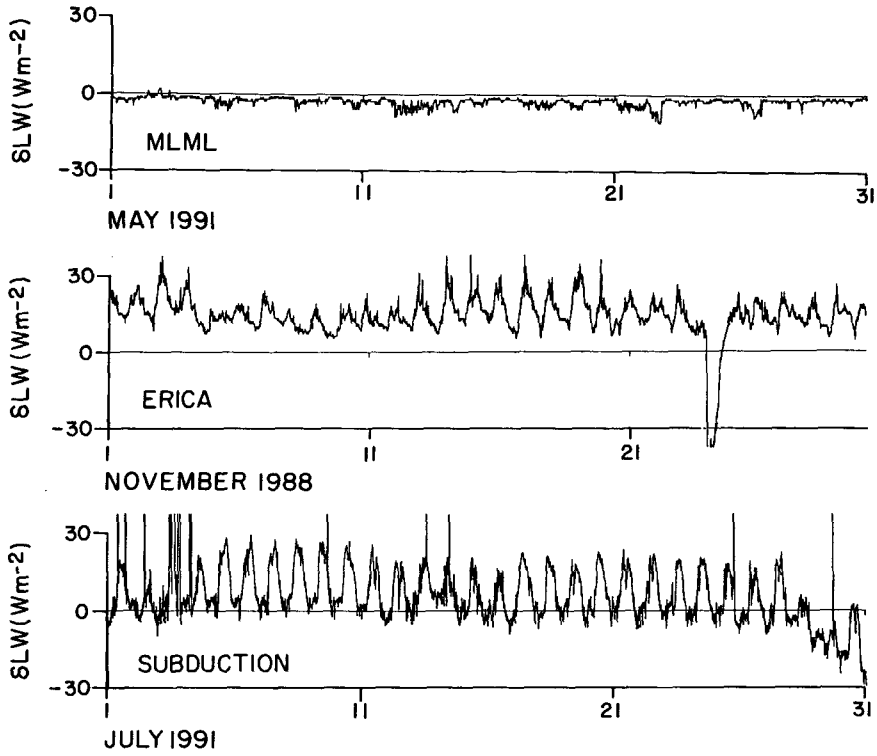

FIG. 20. Enlargements of sections of difference time series (δLW) from MLML ($LW_{184} - LW_{706}$), ERICA ($LW_{707} - LW_{161}$), and Subduction ($LW_{IMET} - LW_{704}$) (top to bottom) illustrating periods when diurnal variability is strong and periods when it is not.

e. Calibration uncertainties

Prior to these deployments, we had little experience with measuring incoming longwave radiation at sea. We anticipated problems from moisture on the domes of the radiometers, whether from condensation, spray, or from water droplets forming around hygroscopic salt crystals, and from solar heating of the radiometer. Thus, in processing the raw data from these four experiments the predeployment calibration values were always used. Plots of the calibration histories of various PIRs (Fig. 19) show the tendency of the calibration values to oscillate about a mean. The average change between successive calibrations of the sensors used in the four experiments was 6.0%. Typically, all PIRs returned to Eppley Laboratory for recalibration on the same day exhibited the same sign and similar magnitude in change in calibration. It is felt that some of the uncertainty in the calibration is due to the calibration procedure itself.

For PreSubduction, the mean calibration sensitivity for PIR 27027 was 4.008 μV $(W\ m^{-2})^{-1}$. Over the available calibration history, the standard deviation of the calibration sensitivity was 0.072 μV $(W\ m^{-2})^{-1}$. The error in the longwave associated with the calibration uncertainty can be estimated as the product of the mean incoming longwave times the standard deviation of the calibration constant divided by the mean calibration constant. For PIR 27026, the estimate of calibration related error is $445.5 \times (0.055/4.055) = 6.0$ W m^{-2}. For PIR 27027, this is 6.6 W m^{-2}. Thus, if the calibration errors are uncorrelated, a difference of approximately 12.6 W m^{-2} might be anticipated between the two records. In PreSubduction, this is smaller than the observed difference due to the failure of the electronics in one VAWR. For ERICA and MLML, where both VAWRs worked well, the differences between the two VAWRs associated with calibration uncertainties were 17.2 and 21.0 W m^{-2}, respectively. The mean differences between the observed time series, 9.0 and 1.7 W m^{-2}, were smaller than these estimates of calibration-related uncertainty. No calibration history exists yet for the IMET longwave module used in Subduction; however, if the standard deviation of the calibration is the same as for the Eppley PIR, the observed mean difference of 4.9 W m^{-2} is smaller than the possible calibration-related error of 13.6 W m^{-2}. Based on the observation that all the PIRs sent for calibration at one time show similar shifts in calibration, it is likely that the calibration errors for two sensors calibrated at the same time are correlated. In this case, summing the error estimates given in Table 4 for individual sensors overestimates the possible error in the difference time series.

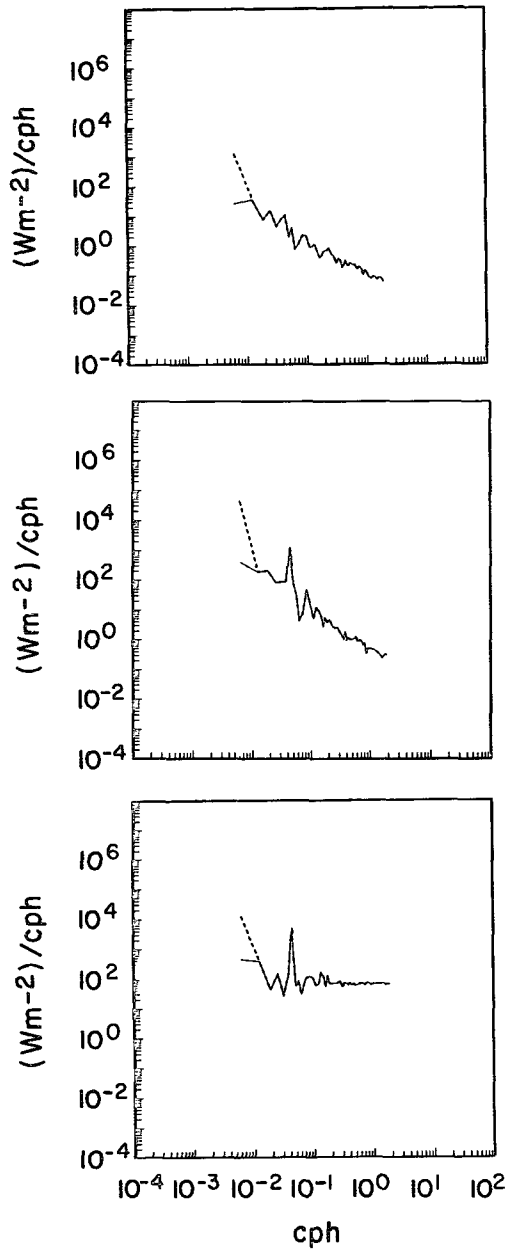

FIG. 21. Spectra of downwelling longwave radiation for 20-day subsets of data from MLML (first 20 days), ERICA (first 20 days), and Subduction (5–25 July) (top to bottom).

f. Radiometer difference uncertainties

The interinstrument difference time series (δLW) from each experiment were analyzed in the time domain to elucidate evidence of instrument error related to variability in environmental conditions. The incoming longwave difference time series from ERICA ($LW_{707} - LW_{161}$) and Subduction ($LW_{IMET} - LW_{704}$) show periods in which diurnal variability was evident (Fig. 20).

However, a scatterplot of the ERICA longwave difference time series against the incoming shortwave recorded by one of the VAWRs did not show a strong correlation. Diurnal variability is not as apparent in the difference time series from MLML ($LW_{184} - LW_{706}$). Spectra for the incoming longwave radiation differences for 20-day subsections of the MLML, ERICA, and Subduction time series are shown in Fig. 21. A strong diurnal peak is obvious for the latter two, but

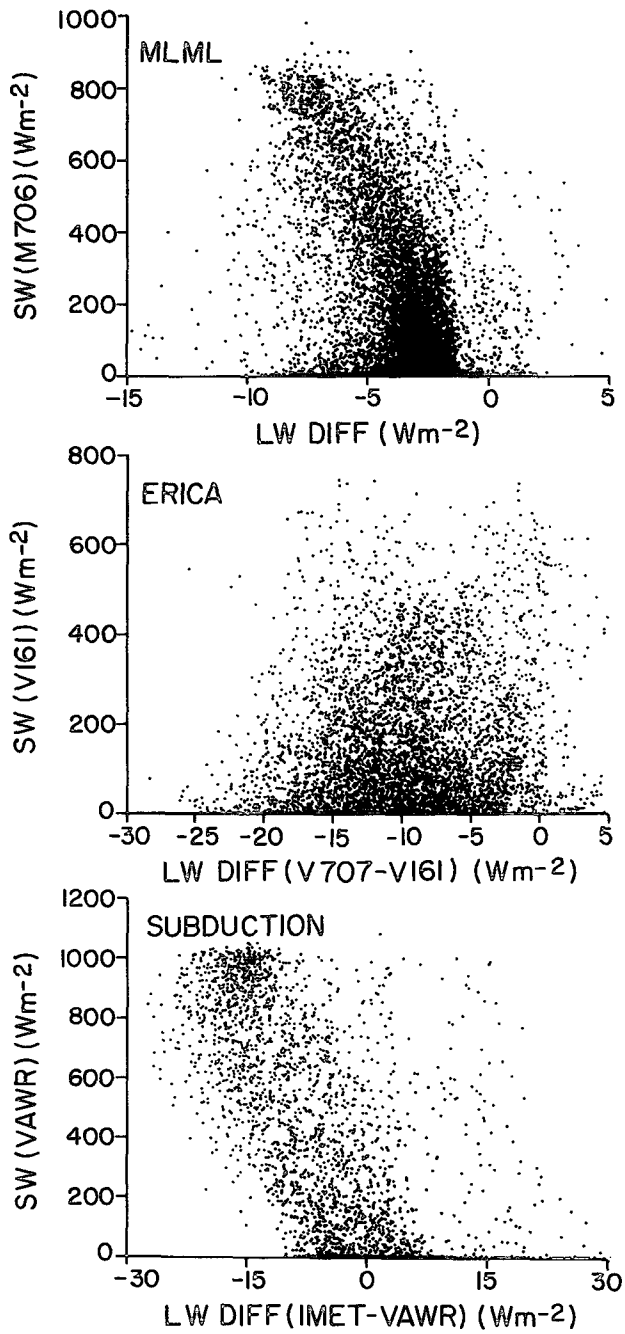

FIG. 22. Scatterplots of longwave difference vs incoming shortwave radiation for MLML, ERICA, and Subduction (top to bottom).

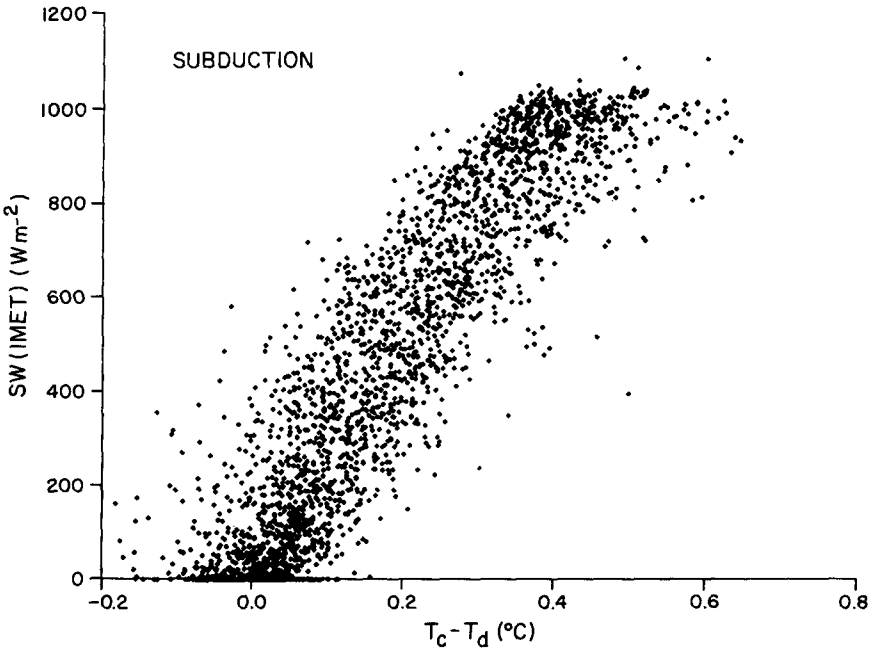

FIG. 23. Scatterplot of the difference in the body and dome temperatures of the IMET longwave radiometer vs the incoming shortwave radiation.

not for MLML. In Subduction, however, the magnitude of the longwave difference did show a dependence on incoming shortwave (Fig. 22) with the largest differences between the two PIRs resulting when the incoming shortwave radiation was largest. The IMET module used in Subduction provided records of the temperature of the body and dome. Gradients in temperature across the radiometer are clearly dependent on the magnitude of the incoming shortwave radiation as indicated in Figure 23.

For ERICA, the dependence of the difference in incoming longwave radiation observed by two sensors on the same buoy was not apparent. In the MLML and Subduction deployments, done during the summer, the difference between the two incoming longwave radiation sensors on the same buoy does increase with increasing shortwave radiation. In MLML, the difference grows to approximately 10 W m^{-2} when incoming shortwave radiation reaches 800 W m^{-2}. In Subduction, the difference grows, with the Eppley PIR values higher than the IMET radiometer, by approximately 17 W m^{-2} when incoming shortwave reaches 1000 W m^{-2}. In the absence of incoming shortwave radiation, the difference in MLML ranged from approximately +2 to −10 W m^{-2}. In Subduction, the nighttime differences ranged from +30 to −8 W m^{-2}, with the IMET longwave module often reading higher than the Eppley PIR.

7. Formulations for the determination of net longwave radiation at the air–sea interface

The net longwave radiation at the sea surface is given by

$$\mathrm{LW}\Updownarrow(0) = \mathrm{LW}\uparrow(0) - \mathrm{LW}\downarrow(0), \quad (14)$$

where LW↑(0) and LW↓(0) are the upwelling and downwelling components of longwave radiation at the sea surface. It is possible to parameterize the upwelling flux in terms of the greybody emissions from the sea surface and the reflected downwelling longwave flux. The upwelling flux LW↑(0) can be evaluated as the sum of the greybody emission of the sea surface and the reflection of the downwelling flux LW↓(0) by the sea surface or

$$\mathrm{LW}\uparrow(0) = \epsilon_{ss}\sigma T_{ss}^4 + (1 - \epsilon_{ss})\mathrm{LW}\downarrow(0), \quad (15)$$

where ϵ_{ss} is the sea surface emissivity and T_{ss} is the temperature of the sea surface that is measured.

The sea surface emissivity, ϵ_{ss}, which is dependent on water temperature and wavelength, is an important parameter. Several studies relevant to the determination of emissivity of freshwater, salt water, and seawater have been done [e.g., pure water: Hall (1964), Mikhaylov and Zolotarev (1970), and Downing and Williams (1975); salt water or seawater: Querry et al. (1972, 1977); both fresh- and seawater: Kropotkin et al. (1966) and Friedman (1969)]. The determination of emissivity is well documented (e.g., Maul 1985). To determine an appropriate value of emissivity, we have computed spectrally weighted emissivity using index of refraction data for fresh- (pure) water [data of Downing and Williams (1975): 3–50 μm], Atlantic seawater [data of Querry et al. (1977): 3–20 μm], and Pacific seawater [data of Querry et al. (1977): 3–20 μm] using the equation

$$\epsilon_{ss} = \frac{\int_{\lambda_1}^{\lambda_2} \epsilon_s(\lambda) B(\lambda, T_{ss}) d\lambda}{\int_{\lambda_1}^{\lambda_2} B(\lambda, T_{ss}) d\lambda}, \quad (16)$$

where λ_1 and λ_2 are the limits of integration (3 and 20 μm or 50 μm as indicated above) and $B(\lambda, T_{ss})$ is Planck's function (e.g., Maul 1985). The numerical integration was done with $\Delta\lambda = 1$ μm. For a sea surface temperature value of $T_{ss} = 300$ K, $\epsilon_{ss} = 0.979$ for pure water, and $\epsilon_{ss} = 0.985$ for Atlantic and Pacific seawater. A range of other values has been forwarded for sea surface emissivity; however, we feel that a value of $\epsilon_{ss} = 0.985 \pm 0.010$ (as based on our literature review and calculations) is a reasonable choice for sea surface longwave radiation determinations.

In application, the downwelling longwave sensor or pyrgeometer is located at some height h above the sea surface. If the absolute humidity, temperature, and downwelling longwave flux at the measurement height h, as well as the sea surface temperature are known, then the effects of the absorption and emission processes upon the redistribution of the longwave heat fluxes may be determined.

It can be shown (Siegel and Dickey 1991) that

$$\mathrm{LW}\Updownarrow(0) = \epsilon_{ss}[\sigma(T_{ss}^4 - \epsilon_f \bar{T}^4) - \mathrm{LW}\downarrow(h)(1 - \epsilon_f)], \quad (17)$$

where $\mathrm{LW}\downarrow(h)$ is measured by a pyrgeometer, ϵ_f is the flux emissivity of the layer, and $\bar{T}$ is the mean temperature of the layer.

To summarize, the variables that must be measured in the field include: the pyrgeometer output voltage, the temperatures of the pyrgeometer's cold junction and dome, shortwave radiation, and air temperature and humidity.

Our analysis suggests that the targeted accuracy goal for the determination of net longwave radiation of ± 10 W m^{-2} is achievable in principle. Details are given in Dickey et al. (1991). It is important to note that the errors estimated by various previous investigators typically did not account for factors such as calibration errors, effects of shortwave heating of the pyrgeometer, the platform height, or the skin temperature effect. In addition, our analysis has incorporated improvements in the theoretical formulations of the heat budget.

8. Summary

The main objective of the present study has been to improve the determination of net longwave radiation based on measurements from buoys and ships. The problem has been approached by reconsidering the basic physics of the problem, by doing extensive laboratory testing and calibrations of longwave sensors, and finally by making field measurements. A theory of operation for a longwave sensor (pyrgeometer) was utilized. It was determined that the instrument's sensitivity, which is weakly dependent upon cold junction temperature, is needed as a parameter for the laboratory calibration of the pyrgeometer (excluding shortwave radiation). The incident shortwave radiation contribution was important for daytime determinations of downwelling longwave radiation for the pyrgeometers used in our work.

The performance of thermopile-based pyrgeometers with silicon domes is problematic, particularly for daytime measurements. Previous investigators have utilized equations that describe pyrgeometer performance under laboratory conditions; however, their equations did not account for conditions found in oceanic field environments. Errors in longwave measurements are due in large part to differences in temperatures measured by the pyrgeometer body and dome compared to the temperature of the atmosphere. Solar radiation significantly increases these temperature differences and is primarily responsible for this error. An evaluation of several calibration methods with emphasis on ground-based pyrgeometers was completed. Different thermopiles, body materials, and body configurations have been utilized and compared. The formulation used here includes a term for shortwave radiation and significantly reduced the error in the downwelling component of net longwave measurements for the pyrgeometers of our study.

Measurements of downwelling longwave radiation are by necessity done at some height above the sea surface. In the past, investigators have ignored the longwave radiant flux contributions of absorption and emission of infrared energy in the region lying between the sensor at some height and the sea surface. For typical marine boundary layer conditions, water vapor may have important consequences upon the regulation of infrared energy fluxes.

Using our recommended pyrgeometer configuration and formulations, the errors associated with the downwelling longwave radiation lead to a relatively moderate contribution to the total uncertainty, ± 10 W m^{-2} for daytime and ± 5 W m^{-2} for nighttime. Provided the sea surface emissivity is uncertain by no more than ± 0.01, then the estimated net longwave heat flux can be determined to within about ± 6 W m^{-2}. The errors estimated by previous investigators typically did not account for factors such as the skin temperature effect or sea surface emissivity uncertainty. Our analysis has incorporated improvements in the theoretical formulations of the heat budget of the pyrgeometer in the calibration of the pyrgeometer. Thus, in practice our recommendations can in fact reduce actual errors substantially.

As a cautionary note, other effects may lead to additional errors that are difficult to quantify. For example, the temperature of the cold junction is taken to be equal to the body temperature–sensing thermistor. This is not necessarily the case, and the two tem-

peratures may not track well because of differences in material thermal properties. During actual deployment, the sensors will tilt in response to ship or buoy motions that may result in downwelling radiant flux measurement errors of several percent (Katsaros and DeVault 1986). The nonuniform spectral response of the pyrgeometer sensor dome may also introduce a few percent error (probably well less than ± 5 W m^{-2}). Another factor is contamination of the pyrgeometer sensor dome. We have attempted to simulate this effect using several application methods of salt water. However, there appeared to be no significant change in the spectral transmission of the pyrgeometer dome. A discussion of this potential effect based on field testing is given in the previous section. Finally, fog or mist conditions can lead to wetting of the dome surface and to anomalous measurements.

Examples of determinations of longwave heat flux from surface buoy observations in four different oceanic regions suggest the following: 1) incoming longwave measurements from buoys are possible and repeatable; two calibrated sensors on the same platform return time series that are in good agreement, 2) uncertainties in the calibration of the Eppley radiometers are significant and appear systematic in that all radiometers calibrated on a given day have similar shifts in calibration, and 3) radiometers deployed during our field study were affected by incoming shortwave radiation when deployed in conditions where solar heating of the sensors and buoy might be anticipated; differences between longwave sensors on the same platform are correlated with the magnitude of the incoming shortwave radiation. The magnitudes of the calibration-related uncertainty and the differences in adjacent sensors associated with shortwave radiation are similar. The good agreement between the pairs of time series obtained from the ERICA, MLML, and Subduction buoys is encouraging. It is not currently possible to conclude how closely present radiometers come to being absolutely correct and the size of the uncertainty associated with the calibration is similar in magnitude to the difference signal observed in the field. Hence, improvement in calibration procedures is needed as well as a radiometer that could be used as a transfer standard to determine if in situ measurements are accurate as well as repeatable.

We conclude that further improvement of the accuracy of net longwave heat flux determinations from buoys and ships will require 1) improved determinations of the sea surface skin temperature, air temperature, and sea surface emissivity, 2) more effective filtering of shortwave radiation by silicon domes, 3) improved calibration methods for longwave sensors, and 4) new sensor technology for the measurement of downwelling longwave radiation. Refinement of measurements and algorithms will require comprehensive measurements, including spectral radiation, in the marine boundary layer (within approximately 10 m of the surface) and in the near-surface ocean from a very stable platform.

Acknowledgments. The present research is part of the Long-lead Time Development Activity for the World Ocean Circulation Experiment (WOCE) supported by Grants OCE87-09614 (TD) and OCE-8709614 (RW) from the National Science Foundation. The work was done in cooperation with Mr. David Hosom of the Woods Hole Oceanographic Institution. Deployment of the buoys and analysis of the longwave radiation data by RW was supported by ONR Grants N00014-9-J-1490 (Subduction), N00014-89-J-1683 (MLML), N00014-90-J-1423 (ERICA), N00014-84-C-0134, and NR083-400 (PreSubduction). The WHOI Contribution Number is 8273. Michael Hamilton is thanked for his assistance with the laboratory work at USC. The help of Nancy Brink and Kelan Huang in the plotting and analysis of the data is gratefully acknowledged. Discussions with Kristina Katsaros and John Foot greatly benefited our study.

REFERENCES

Alados-Arboledas, L., J. Vida, and J. I. Jimenez, 1988: Effects of solar radiation on the performance of pyrgeometers with silicon domes. *J. Atmos. Oceanic Technol.*, **5**, 666–670.

Albrecht, B., and S. K. Cox, 1977: Procedures for improving pyrgeometer performance. *J. Appl. Meteor.*, **16**, 188–197.

——, M. Poellot, and S. K. Cox, 1974: Pyrgeometer measurements from aircraft. *Rev. Sci. Instrum.*, **45**, 33–38.

Allsup, G., 1990: A standardized electronics package for IMET sensor development. *IEEE Proc., OCEANS '90*, 164–168.

Bradley, S. G., and R. G. Gibson, 1982: On the use of pyrgeometers in cloud. *J. Appl. Meteor.*, **21**, 1155–1159.

Breon, F.-M., R. Frouin, and C. Gautier, 1991: Downwelling longwave irradiance at the ocean surface: An assessment of in situ measurements and parameterizations. *J. Appl. Meteor.*, **30**, 17–31.

Brogniez, G., J. Buriez, J. Vanhoutte, and Y. Fouquart, 1986: An improvement of the calibration of the Eppley pyrgeometer for the case of airborne measurements. *Beitr. Phys. Atmos.*, **4**, 538–551.

Bunker, A. F., 1976: Computations of surface energy flux and annual air–sea interaction cycles of the North Atlantic Ocean. *Mon. Wea. Rev.*, **104**, 1122–1140.

Campbell, G. S., J. N. Mugaas, and J. R. King, 1978: Measurement of long-wave radiant flux organismal energy budgets: A comparison of three methods. *Ecology*, **59**, 1277–1281.

Chou, M.-D., 1985: Surface radiation in the tropical Pacific. *J. Climate Appl. Meteor.*, **24**, 83–92.

Crescenti, G. H., and R. A. Weller, 1989: Improved meteorological measurements from buoys and ships (IMET): Preliminary comparison of precipitation sensors. Woods Hole Oceanographic Institution Tech. Rep. WHOI-89-44, IMET TR-89-01, 32 pp. [Available from WHOI, Woods Hole, MA 02543.]

——, and R. E. Payne, 1991: Evaluation of two types of thin film capacitive relative humidity sensors for use on buoys and ships. *Seventh Symp. on Meteorological Observations and Instrumentation*, New Orleans, Amer. Meteor. Soc., 125–128.

——, and R. A. Weller, 1992: Analysis of surface fluxes in the marine atmospheric boundary layer in the vicinity of rapidly intensifying cyclones. *J. Appl. Meteor.*, **31**, 831–848.

——, R. E. Payne, and R. A. Weller, 1989a: Improved meteorological measurements from buoys and ships (IMET): Preliminary comparison of pyranometers. Woods Hole Oceanographic In-

stitution Tech. Rep. WHOI-89-47, IMET TR-89-04, 30 pp. [Available from WHOI, Woods Hole, MA 02543.]

——, ——, and ——, 1989b: Improved meteorological measurements from buoys and ships (IMET): Preliminary comparison of solar radiation air temperature shields. Woods Hole Oceanographic Institution Tech. Rep. WHOI-89-46, IMET TR-89-03, 53 pp. [Available from WHOI, Woods Hole, MA 02543.]

——, R. A. Weller, D. S. Hosom, and K. E. Prada, 1989c: Improved meteorological measurements from buoys and ships (IMET): Preliminary analysis of solar radiation and motion data from IMET test buoy. Woods Hole Oceanographic Institution Tech. Rep. WHOI-89-45, IMET TR-89-02, 38 pp. [Available from WHOI, Woods Hole, MA 02543.]

——, R. E. Payne, and R. A. Weller, 1990: Improved meteorological measurements from buoys and ships (IMET): Preliminary comparison of humidity sensors. Woods Hole Oceanographic Institution Tech. Rep. WHOI-90-18, IMET TR-90-02, 57 pp. [Available from WHOI, Woods Hole, MA 02543.]

——, D. S. Hosom, and R. E. Payne, 1991a: Development of an intelligent chilled mirror dew point sensor. *Seventh Symp. on Meteorological Observations and Instrumentation,* New Orleans, Amer. Meteor. Soc., 297–302.

——, S. A. Tarbell, and R. A. Weller, 1991b: A compilation of moored current meter data and wind recorder data from the severe environment from the Severe Environment Surface Mooring (SESMOOR) Volume XLIII. Woods Hole Oceanographic Institution Tech. Rep., WHOI-91-18, 59 pp. [Available from WHOI, Woods Hole, MA 02543.]

Dean, J. P., and R. C. Beardsley, 1988: A vector-averaging wind recorder (VAWR) system for surface meteorological measurements in CODE (Coastal Ocean Dynamics Experiment). Woods Hole Oceanographic Institution Tech. Rep. WHOI-88-20, 74 pp. [Available from WHOI, Woods Hole, MA 02543.]

Dickey, T. D., and D. V. Manov, 1991: Theory of thermopile-based pyrgeometers for the measurement of downwelling longwave radiation. Woods Hole Oceanographic Institution Tech. Rep. IMET TR-91-3-B, 16 pp. [Available from WHOI, Woods Hole, MA 02543.]

——, ——, and D. A. Siegel, 1991: The determination of net longwave heat flux at the air–sea interface. Woods Hole Oceanographic Institution Tech. Rep. IMET TR-90-3-D, 34 pp. [Available from WHOI, Woods Hole, MA 02543.]

Donelan, M. A., 1990: Air–sea interaction. *The Sea,* Vol. 19, B. LeMauhaute and D. Hines, Eds., John Wiley and Sons, 239–292.

Dorman, C. E., C. A. Paulson, and W. H. Quinn, 1974: An analysis of 20 years of meteorological and oceanographic data from ocean station *N. J. Phys. Oceanogr.,* **4,** 645–653.

Downing, H. D., and D. Williams, 1975: Optical constants of water in the infrared. *J. Geophys. Res.,* **80,** 1656–1661.

Enz, J. W., J. C. Klink, and D. G. Baker, 1975: Solar radiation effects on pyrgeometer performance. *J. Appl. Meteor.,* **14,** 1297–1302.

Eppley Laboratory, Inc., 1971: Instrumentation for the measurement of the components of solar and terrestrial radiation. Eppley Laboratory, 31 pp. [Available from Eppley Laboratory, Inc., 12 Scheffield Ave., Newport, RI 02840.]

——, 1989: Instrumentation for the measurement of the components of solar and terrestrial radiation. Eppley Laboratory, 12 pp. [Available from Eppley Laboratory, Inc., 12 Scheffield Ave., Newport, RI 02840.]

Foot, J. S., 1986: A new pyrgeometer. *J. Atmos. Oceanic Technol.,* **3,** 363–370.

Friedman, D., 1969: Infrared characteristics of ocean water (1.5–15 μ). *Appl. Opt.,* **8,** 2073–2078.

Fung, I. Y., D. E. Harrison, and A. A. Lacis, 1984: On the variability of the net longwave radiation at the ocean surface. *Rev. Geophys. Space Phys.,* **22,** 177–193.

Hadlock, R., and C. W. Kreitzberg, 1988: The Experiment on Rapidly Intensifying Cyclones over the Atlantic (ERICA) field study: Objective and plans. *Bull. Amer. Meteor. Soc.,* **69,** 1309–1320.

Hall, F. F., 1964: The polarized emissivity of water in the infrared. *Appl. Opt.,* **3,** 781–782.

Halldin, S., and A. Lindroth, 1992: Errors in net radiometry: Comparisons and evaluation of six radiometer designs. *J. Atmos. Oceanic Technol.,* **9,** 762–783.

Hinton, A., 1990: Air and sea temperature measurements for IMET. *IEEE Proc. OCEANS '90,* 169–171.

Hinzpeter, H., 1980: Atmospheric radiation instruments. *Air–Sea Interaction Instruments and Methods,* F. Dobson, L. Hasse, and R. Davis, Eds., Plenum Press, 491–508.

Hosom, D. S., G. H. Crescenti, C. L. Winget, S. Weisman, D. P. Doucet, and J. F. Price, 1991: An intelligent chilled mirror humidity instrument. *J. Atmos. Oceanic Technol.,* **8,** 585–596.

Katsaros, K. B., 1980: Radiative sensing of sea surface temperature. *Air–Sea Interaction,* F. Dobson, L. Hasse, and R. Davis, Eds., Plenum Press, 293–317.

——, 1990: Parameterization schemes and models for estimating the specific radiation budget. *Surface Waves and Fluxes,* Vol. 2, G. L. Geernaert and W. J. Plant, Eds., Kluwer Academic, 339–368.

——, and J. E. D. DeVault, 1986: On irradiance measurement errors at sea due to tilt of pyranometers. *J. Atmos. Oceanic Technol.,* **3,** 740–745.

Kropotkin, M. A., B. P. Kozyrev, and V. A. Zaitsev, 1966: Infrared reflection spectra of sea and fresh water and of several aqueous solutions. *Izv. Atmos. Oceanic Phys.,* **2,** 434–435.

Lind, R. J., and K. B. Katsaros, 1986a: A model of longwave irradiance for use with surface observations. *J. Appl. Meteor.,* **21,** 1015–1023.

——, and ——, 1986b: Radiation measurements and model results from R/V *Oceanographer* during STREX 1980. *J. Geophys. Res.,* **91,** 13 308–13 314.

——, ——, and M. Gube, 1984: Radiation budget components and their parameterization in JASIN. *Quart. J. Roy. Meteor. Soc.,* **110,** 1061–1071.

MacWhorter, M. A., and R. A. Weller, 1991: Error in measurements of incoming shortwave radiation made from ships and buoys. *J. Atmos. Oceanic Technol.,* **8,** 108–117.

Manov, D., 1991: Calibration methods for pyrgeometers. Woods Hole Oceanographic Institution Tech. Rep. IMET TR-91-3-B, 80 pp. [Available from WHOI, Woods Hole, MA 02543.]

Maul, G. A., 1985: *Introduction to Satellite Oceanography.* Matinus Nijhoff, 606 pp.

Mikhaylov, B. A., and V. M. Zolotarev, 1970: Emissivity of liquid water. *Izv. Acad. Sci. USSR, Atmos. Oceanic Phys.,* **6,** 96–97.

Paltridge, G. W., 1969: A net long-wave radiometer. *Quart. J. Roy. Meteor. Soc.,* **95,** 635–638.

——, 1970: Day-time long-wave radiation from the sky. *Quart. J. Roy. Meteor. Soc.,* **96,** 645–653.

Payne, R. E., 1974: A buoy-mounted meteorological package. Woods Hole Oceanographic Institution Tech. Rep. WHOI-74-40, 32 pp. [Available from WHOI, Woods Hole, MA 02543.]

——, G. H. Crescenti, and R. A. Weller, 1989: Improved meteorological measurements from buoys and ships (IMET): Preliminary report on barometric pressure sensors. Woods Hole Oceanographic Institution Tech. Rep. WHOI-89-49, IMET TR-89-05, 43 pp. [Available from WHOI, Woods Hole, MA 02543.]

Prada, K. E., 1990: Improved meteorological measurements from buoys and ships (IMET): Preliminary conventions and standards, data and file formats. Woods Hole Oceanographic Institution Tech. Rep. WHOI-90-10, IMET TR-90-01, 11 pp. [Available from WHOI, Woods Hole, MA 02543.]

——, D. Hosom, and A. Hinton, 1989: Improved meteorological measurements from ships and buoys. *IEEE Proc., OCEANS '89,* **5,** 1410–1415.

——, ——, and ——, 1990: Improved meteorological measurements from buoys and ships. *Proc. Marine Instrumentation '90,* San Diego, Marine Technology Society, 178–182.

Querry, M. R., R. C. Waring, W. E. Holland, G. M. Hale, and W. Nijm, 1972: Optical constants in the infrared for aqueous solutions of NaCl. *J. Opt. Soc. Amer.,* **62,** 849–855.

——, W. E. Holland, R. C. Waring, L. M. Earls, and M. D. Querry, 1977: Relative reflectance and complex refractive index in the infrared for saline environmental waters. *J. Geophys. Res.*, **82,** 1425–1433.

Reed, R. K., 1976: On estimation of net long-wave radiation from the oceans. *J. Geophys. Res.*, **81,** 5793–5794.

——, and D. Halpern, 1975: Insolation and net long-wave radiation off the Oregon coast. *J. Geophys. Res.*, **80,** 839–844.

Ryznar, E., and M. R. Weber, 1982: Comments on "The performance of pyrgeometers with silicon domes." *J. Appl. Meteor.*, **21,** 1208–1212.

Siegel, D. A., and T. D. Dickey, 1986: Variability of net longwave radiation over the eastern North Pacific Ocean. *J. Geophys. Res.*, **91,** 7657–7666.

——, and ——, 1991: Longwave heat fluxes at the sea surface: Influence of the marine boundary layer. Woods Hole Oceanographic Institution Tech. Rep. IMET TR-91-3-C, 30 pp. [Available from WHOI, Woods Hole, MA 02543.]

Simpson, J. J., and C. A. Paulson, 1979: Mid-ocean observations of atmospheric radiation. *Quart. J. Roy. Meteor. Soc.*, **105,** 487–502.

Smith, S. D., and F. W. Dobson, 1984: The heat budget at OWS Bravo. *Atmos. Ocean.*, **22,** 1–22.

Smith, W. L., S. K. Cox, and V. Glover, 1988: A thermopile temperature sensitivity calibration procedure for Eppley broadband radiometers. NCAR Tech. Note, NCAR/TN-320+STR, 14 pp. [Available from Atmospheric Technology Division, National Center for Atmospheric Research, P.O. Box 3000, Boulder, CO 80303.]

Weiss, A., 1981: On the performance of pyrgeometers with silicon domes. *J. Appl. Meteor.*, **20,** 962–965.

Weller, R. A., and D. S. Hosom, 1989: Improved meteorolcgical measurements from buoys and ships for the World Ocean Circulation Experiment. *IEEE Proc., OCEANS '89,* **5,** 1410–1415.

——, D. L. Rudnick, R. E. Payne, J. P. Dean, N. J. Pennington, and R. P. Trask, 1990: Measuring near-surface meteorology over the ocean from an array of surface moorings in the subtropical convergence zone. *J. Atmos. Oceanic Technol.*, **7,** 85–103.

——, M. A. Donelan, M. G. Briscoe, and N. E. Huang, 1991a: Riding the crest: A tale of two wave experiments. *Bull. Amer. Meteor. Soc.*, 163–183.

——, D. S. Hosom, K. E. Prada, and G. H. Crescenti, 1991b: Improved meteorological instruments and data acquisition systems for buoys and ships. *Seventh Symp. on Meteorological Observations and Instrumentation,* New Orleans, Amer. Meteor. Soc., 129–133.

WOCE, 1985: WOCE global air–sea interaction fields. U.S. WOCE Tech. Rep. No. 1, 36 pp. [Available from W. G. Large, National Center for Atmospheric Research, P.O. Box 3000, Boulder, CO, 80303.]

——, 1989: The U.S. contribution to WOCE numerical modeling. U.S. WOCE Planning Rep. No. 14, 37 pp. [Available from U.S. WOCE Office, Texas A&M University, College Station, TX 77843.]